

This work was written as part of one of the author's official duties as an Employee of the United States Government and is therefore a work of the United States Government. In accordance with 17 U.S.C. 105, no copyright protection is available for such works under U.S. Law.

Public Domain Mark 1.0

<https://creativecommons.org/publicdomain/mark/1.0/>

Access to this work was provided by the University of Maryland, Baltimore County (UMBC) ScholarWorks@UMBC digital repository on the Maryland Shared Open Access (MD-SOAR) platform.

**Please provide feedback**

Please support the ScholarWorks@UMBC repository by emailing [scholarworks-group@umbc.edu](mailto:scholarworks-group@umbc.edu) and telling us what having access to this work means to you and why it's important to you. Thank you.

TOPICAL REVIEW

## Sustained Spheromak Physics Experiment (SSPX): design and physics results

To cite this article: E B Hooper *et al* 2012 *Plasma Phys. Control. Fusion* **54** 113001

View the [article online](#) for updates and enhancements.

### You may also like

- [Effect of geometric and magnetic boundary conditions on magnetic islands in 3D force-free ideal MHD equilibria](#)  
T.E. Benedetti and C.J. Hansen
- [Relativistic Magnetic Explosions](#)  
Maxim V. Barkov, Praveen Sharma, Konstantinos N. Gourgouliatos et al.
- [Successive Interacting Coronal Mass Ejections: How to Create a Perfect Storm](#)  
G. J. Koehn, R. T. Desai, E. E. Davies et al.

## TOPICAL REVIEW

# Sustained Spheromak Physics Experiment (SSPX): design and physics results

**E B Hooper<sup>1</sup>, R H Bulmer<sup>1,6</sup>, B I Cohen<sup>1</sup>, D N Hill<sup>1</sup>, C T Holcomb<sup>1</sup>,  
B Hudson<sup>2</sup>, H S McLean<sup>1</sup>, L D Pearlstein<sup>1,6</sup>, C A Romero-Talamás<sup>3</sup>,  
C R Sovinec<sup>4</sup>, B W Stallard<sup>1,6</sup>, R D Wood<sup>1</sup> and S Woodruff<sup>5</sup>**

<sup>1</sup> Lawrence Livermore National Laboratory, PO Box 808, Livermore, CA 94550, USA

<sup>2</sup> Center for Energy Research, University of California-San Diego, 9500 Gilman Dr, La Jolla, CA 92093-0417, USA

<sup>3</sup> Institute for Research in Electronics and Applied Physics, University of Maryland, College Park, MD 20742, USA

<sup>4</sup> Department of Engineering Physics, University of Wisconsin-Madison, Madison, WI 53706-1609, USA

<sup>5</sup> Woodruff Scientific Inc., 4501 Shilshole Ave. NW, Seattle, WA 98107, USA

E-mail: [hooper1@llnl.gov](mailto:hooper1@llnl.gov)

Received 12 July 2012, in final form 4 September 2012

Published 9 October 2012

Online at [stacks.iop.org/PPCF/54/113001](http://stacks.iop.org/PPCF/54/113001)

## Abstract

The Sustained Spheromak Physics Experiment (SSPX) was a high-temperature ( $T_e$  up to 0.5 keV) spheromak formed by coaxial helicity injection (CHI) and with plasma duration of a few milliseconds following the high-current formation stage. Clean walls and low impurity operation were obtained by a combination of baking, discharge cleaning and titanium deposition on the walls, allowing the generation of high-quality plasmas. Resistive-magnetohydrodynamic simulations, benchmarked to the experiment, were used to elucidate the physics. The detailed characteristics of the  $n_\phi = 1$  toroidal mode associated with CHI were determined as was the physics of the nonlinear current drive and magnetic reconnection that formed and sustained the spheromak. If the helicity injection rate was reduced following formation the plasma became relatively quiescent and magnetic surfaces formed. The measured thermal diffusivity in the core was as low as  $\sim 1 \text{ m}^2 \text{ s}^{-1}$ . However, reconnection events during buildup or sustainment of the plasma current by CHI were found to open magnetic surfaces throughout the plasma allowing rapid energy loss to the walls. As a result, experiments and simulations in SSPX found no path to simultaneous sustainment by CHI and good energy confinement. Additional physics results are also presented in this review.

(Some figures may appear in colour only in the online journal)

## 1. Introduction

The Sustained Spheromak Physics Experiment (SSPX) was a 1 m diameter spheromak formed by coaxial helicity injection (CHI) and used to study spheromak physics with a focus on sustained, long-pulse operation and the possibility of achieving steady-state or quasi-steady state operation with good energy confinement. The results of the experimental program and closely coupled modeling and resistive-magnetohydrodynamics (MHD) simulations are

presented here including a comparison with other spheromak studies where appropriate. During its operation SSPX achieved quasi-steady state, volume-averaged beta of a few percent; suppression of magnetic turbulence to below 1%; observation of confinement, island formation and toroidal modes consistent with good flux surfaces; peak electron temperatures in the core of 0.5 keV; and core thermal diffusivities that dropped rapidly with increasing electron temperature, reaching as low as  $1 \text{ m}^2 \text{ s}^{-1}$ .

Magnetized plasma rings were first investigated by Alfvén *et al* [1]. The name ‘spheromak’ was applied to

<sup>6</sup> Retired.

a low-aspect-ratio, compact torus configuration with safety-factor,  $q$ , less than unity by Bussac *et al* [2] and by Rosenbluth and Bussac [3] who investigated its MHD stability. Although originally applied to the limiting case of a force-free plasma with constant current density per unit magnetic flux,  $\lambda = j \cdot B/B^2$ , the name is now applied without these restrictions. Extensive experimental and theoretical research on spheromaks was initiated in the 1980s. Spheromaks were formed in experiments using a variety of methods: flux-core induction [4], combined theta-pinch and  $z$ -pinch [5, 6], helicity injection from a coaxial, magnetized gun [7–9], a conical  $\theta$ -pinch [10], and a kinked  $z$ -pinch [11]. The physics was developed extensively with experiments on CTX [9]. Subsequently, the helicity-injected experiments SPHEX [12] and FACT [13] further extended the understanding of spheromak physics, and the HIT-SI experiment [14] is utilizing an inductively driven helicity injection technique. A review of this research up to 1994 can be found in a review paper by Jarboe [15]. Bellan subsequently published a book which includes a good introduction, especially into the theory of spheromaks [16].

The configuration offers a variety of interesting physics and engineering features. Compact torus configurations such as the spheromak require no external toroidal magnetic field and thus no central column, resulting in a simply connected containment volume which could make a relatively simple fusion reactor. As  $q < 1$  its MHD physics complements those in the tokamak with  $q > 1$  and in the reversed-field pinch (RFP) which has  $q < 1$  with a reversal near the edge. The spheromak has a low aspect ratio so that toroidal effects are highly important. Because of the absence of a large, external toroidal magnetic field, magnetic self-organization is important, and helicity provides a paradigm for describing the configuration, as in the RFP. Taylor [17, 18] showed that force-free, constant- $\lambda$  configurations result from the minimization of the plasma magnetic energy subject to the constraint of constant total helicity, interpreted as a measure of linked magnetic fluxes; this is expected to occur when the  $\lambda$  profile flattens due to turbulence resulting from tearing modes. The fully relaxed plasma is often called the ‘Taylor state.’

Experimentally, spheromaks usually operate with non-uniform  $\lambda$  and are not fully relaxed. Indeed, the non-uniformity is essential for current drive. However, the spheromak’s low  $q$  and high plasma current have proved difficult to maintain in a stable state with good confinement. Determining the extent to which helicity current drive is consistent with good confinement was an important goal of SSPX.

SSPX was designed to operate at high bias poloidal magnetic flux, high injection current, and multi-millisecond pulse lengths, and to generate a high-quality plasma at low impurity levels. The experiment had a flux-conserving boundary (flux conserver) with a radius,  $R = 0.5$  m and height,  $h = 0.5$  m, and had a 1.2 cm thick conducting copper shell with the plasma-facing surface coated with tungsten. Extensive wall conditioning was carried out, including baking after vents, discharge conditioning, and regular gettering with titanium. The result was a low level of impurities and discharges with peak temperatures as high as 0.5 keV despite the small minor

radii  $\sim 0.2$  m. Power-balance measurements of the thermal diffusivity in the plasma core under operating conditions such that magnetic fluctuations were low were found to be comparable to tokamak L-mode values.

During nearly a decade of operations, the SSPX results found no evidence that it is possible to sustain the plasma configuration against resistive decay and simultaneously maintain good-confinement properties; this conclusion is consistent with theoretical predictions that helicity will not transport across closed magnetic surfaces [19–21]. The results summarized in this paper demonstrate that the instabilities that give rise to current transport seriously enhance energy and particle transport, tearing up flux surfaces and destroying regions of good confinement. The conclusions were supported by detailed comparison of experimental data with resistive-MHD simulations—it is shown that the large cathode-voltage pulses observed during the plasma buildup or current-sustainment phases were largely due to magnetic-reconnection events which resulted in relaxation of the current profile and the generation of plasma current. The dynamo was examined in considerable detail and the resulting current-drive efficiency documented. However, one of the strong conclusions from this body of research is that good confinement and sustainment of toroidal current in a spheromak by helicity injection from electrodes are mutually exclusive, leading to a proposal of quasi-steady state or ‘pulsed-refluxing’ scenarios for future research.

Interpretation of the experimental results was supported by extensive numerical calculations with two codes: Corsica [22, 23] and NIMROD [24]. Corsica is based on solutions of the Grad–Shafranov equation including edge currents resulting from helicity and current injection from a ‘gun’. Corsica includes integrated physics models for Ohmic heating, transport and other important physics. It was also used to invert edge magnetic probe measurements and to analyze other experimental data. NIMROD is a 3D, resistive-MHD code used for SSPX to understand the role of the current profile and magnetic fluctuations in energy confinement, magnetic reconnection and the dynamo, and other physics.

Details of the experiment and results are provided in the following sections. Section 2 describes the design and operation of the experiment, section 3 details experimental and computational results, and section 4 includes discussion and conclusions.

## 2. SSPX design and operation

### 2.1. Design overview

Figure 1(a) shows a cutaway illustration of the SSPX flux conserver and inner electrode suspended from a large-diameter flange. This structure was placed inside a large vacuum vessel, with a vacuum seal between this flange and the vessel top. The vessel provided an effective pumping system for the duration of the spheromak (few ms maximum). Figure 1(b) is a drawing along with an example of axisymmetric flux surfaces calculated for the spheromak.

The SSPX facility was comprised of mechanical, electrical, diagnostic and auxiliary systems. Mechanical

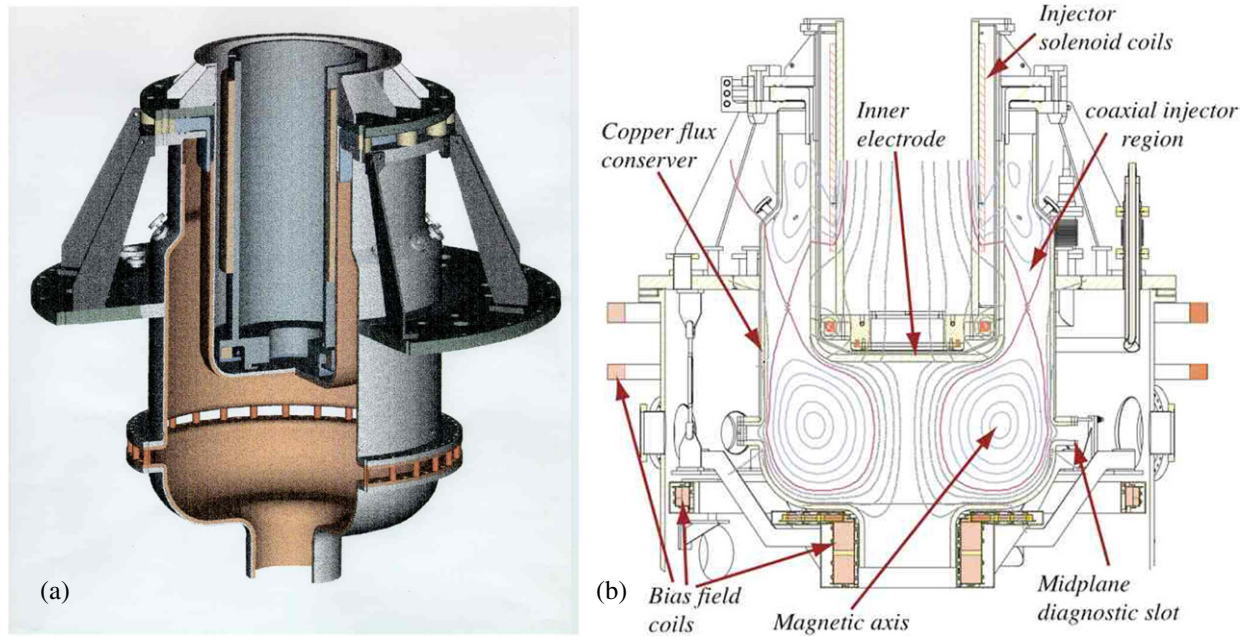


**Figure 1.** (a) Illustration of the flux conserver and inner electrode. (b) Drawing identifying important features and a calculation of typical, axisymmetric magnetic flux surfaces. The coaxial region is called the ‘gun’; current drawn between the inner electrode (cathode) and outer flux conserver (anode) in the presence of a bias (vacuum) magnetic field forms the spheromak. Gas valves are mounted on the small flanges where the outer gun wall bends at  $\approx 45^\circ$ .

systems included the inner electrode and flux conserver, the gas injection system, the vacuum vessel and pumping system and the nine magnet coils that setup the bias magnetic fields prior to a discharge. Electrical systems included four high-energy capacitor banks and dc power supplies for the magnet coils. A large array of diagnostics provided measurements, including the discharge current and voltage, wall magnetic fields, plasma electron density and temperature, and spectroscopy measurements of impurity ions. Important auxiliary systems were the wall conditioning and baking systems. Brief descriptions of these systems are provided here and in appendix A.

## 2.2. Electrode and flux-conserver geometry

The injector consists of three main pieces: an inner electrode, outer electrode and lower flux conserver. The inner and outer electrodes are coaxial with the inner having a diameter of 0.68 m. The outer electrode is 0.88 m diameter at the top next to an alumina insulator and continues down at constant diameter to the gas valve injection ring where it expands outward to a diameter of 1.0 m. The reason for the reduced gap between the outer and inner electrodes at the top was to minimize the plasma there, as current flowing there will tend to be ‘ejected’ into the larger coaxial gap downstream. This effect and careful design of the insulator between the two electrodes resulted in reliable, high-voltage operation without electrical breakdown across the insulator. The outer electrode continues at 1 m diameter down to the flux-conserver midplane where it connects, via a large flanged joint, to the lower flux conserver, which curves inward ending with a smaller diameter (0.3 m) open-ended cylindrical divertor region which also provides additional area for vacuum pumping. The flanges are connected with 32 posts arranged

azimuthally to provide an opening at the midplane of the flux-conserver region for diagnostic access and vacuum pumping. The posts were designed with high-current joints to provide low-resistance and low-inductance axial current flow. The electrodes and flux conserver were constructed of 1.9 cm thick copper to freeze-in the normal component of the bias magnetic field during the several ms-long plasma discharge. The copper was backed by stainless-steel for strength and coated with a thin layer of tungsten [25] to minimize sputtering. Discharge cleaning was used each day, and titanium was deposited on the tungsten during operation to provide a clean, plasma-facing surface [26, 27].

## 2.3. Magnet coils and vacuum flux-shaping capability

Nine poloidal magnet coils, seen in figure 1(b), were incorporated in SSPX to provide a wide-range of bias flux shapes. Past CHI spheromaks have operated with a radial bias magnetic field largely confined to the coaxial gun. A large discharge current is required to overcome the magnetic tension in the bias field and inject plasma into the flux conserver. This current, known as the ‘bubble-burst’ current [28], is sufficiently high that the spheromak plasma is unstable while the current is maintained. To allow operation at currents below this limit, the bias magnetic coils were designed to allow flux to be pulled out of the gun. In addition, considerable shaping capability was provided. The resulting configuration had a main solenoid and two trim coils inside the inner electrode, plus six other coils outside the flux conserver. Examples of the possible bias magnetic configuration are shown in figure 2. The maximum available magnetic flux was about 75 mWb, although most discharges used  $\sim 30$  mWb to minimize the between-shot cooling time. Except where otherwise noted,



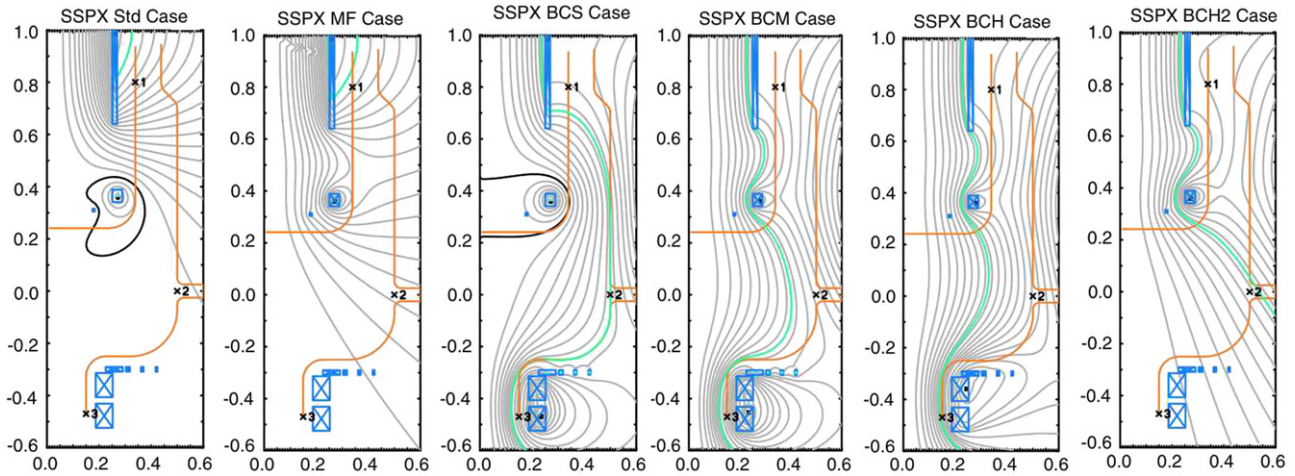


**Figure 2.** Considerable flexibility for the initial vacuum magnetic flux shapes was available in SSPX. Flux configurations based on the SSPX magnet coils were determined by Grad–Shafranov calculations using the Corsica code; they were also the starting point for plasma equilibria and evolution modeling including the spheromak currents.

the ‘SSPX MF’ configuration was used in the physics studies reported in this review.

#### 2.4. Main discharge cap banks

There were three main discharge banks on SSPX. A simple schematic of the power supply is presented in section A1 of the appendix. A formation bank and sustainment bank were installed initially with the modular bank added later. The formation bank supplied a high-voltage pulse to breakdown the injected gas. The sustainment bank (a pulse-forming network) provided an approximately constant current for approximately 2.5 ms. The modular bank allowed more flexible waveforms and extended the pulse for several more ms, depending on the charges on the individual capacitors.

#### 2.5. Gas injection system

Control of the timing and amount of injected gas was important for high-quality operation of SSPX. Gas was injected high in the coaxial gun from eight valves mounted circumferentially where the electrodes slope out from 34 to 50 cm radius. (See the caption to figure 1.) The valves were magnetic hammer-type valves which opened in  $\sim 100 \mu\text{s}$ , dumping a fixed plenum volume of gas at pre-determined pressure. Valves were held closed with a pressure of 200 psig acting on the top piston (area  $\sim 1 \text{ cm}^2$ ). Valves empty at a rate consistent with critical flow. The total volume of eight valves initially was  $1.54 \text{ cm}^3$ . In 2005, four valves were modified to increase injection rate. These valves had a plenum volume of  $0.8916 \text{ cm}^3$  each and total injection volume for four of each type totaled  $1.13 \text{ cm}^3$ . Maximum gas pressure for the valves is 350 psia. Gases used include  $\text{H}_2$ ,  $\text{D}_2$  and  $\text{He}$ ; unless otherwise indicated, the discharges discussed in this review used  $\text{H}_2$ .

The eight valves were fired by the gas-valve capacitor bank, which was comprised of two independent sections with dummy loads that allowed firing any combination of valves at two separate times as well as all eight valves together. Each section of the gas valve bank was a  $400 \mu\text{F}$  high-voltage

capacitor, charged to 3.4 kV and switched with an ignitron. Electrical current per gas valve peaked at approximately 8–10 kA and rang several times with a period of about  $150 \mu\text{s}$ . Pulsed-magnetic coils in each valve were tape-wound with an inductance of  $\sim 8 \mu\text{H}$ .

#### 2.6. Wall conditioning, and impurity control

The vacuum system and pertinent vessel volumes are summarized in section A2 of the appendix. Considerable care was focused on obtaining a clean system, using hard seals (with the exception of the seal between the electrode-supporting flange and vacuum vessel) and oil-free pumps. A base pressure  $< 10^{-9}$  Torr was typically achieved before physics operations commenced. See the appendix for measurements used to evaluate the results of the wall and vacuum conditioning.

#### 2.7. Diagnostic systems

SSPX had an extensive array of diagnostics to measure the basics plasma parameters, many installed by collaborators [29]. The primary instruments are shown in the overview in figure 3 and listed in appendix A

### 3. Physics results

#### 3.1. Overview

Following a brief description of typical operating parameters in section 3.2, studies of spheromak formation are described in section 3.3. The role and nature of the  $n_\phi = 1$  toroidal mode are discussed from the perspectives of experiment and resistive-MHD simulations. Section 3.4 extends this study, presenting the evidence for reconnection events which convert injected toroidal magnetic flux into poloidal flux. Field lines are found to open at each reconnection event, causing rapid transport of electron energy to the walls and significantly limiting the temperature. Experimental measurements of the attainable

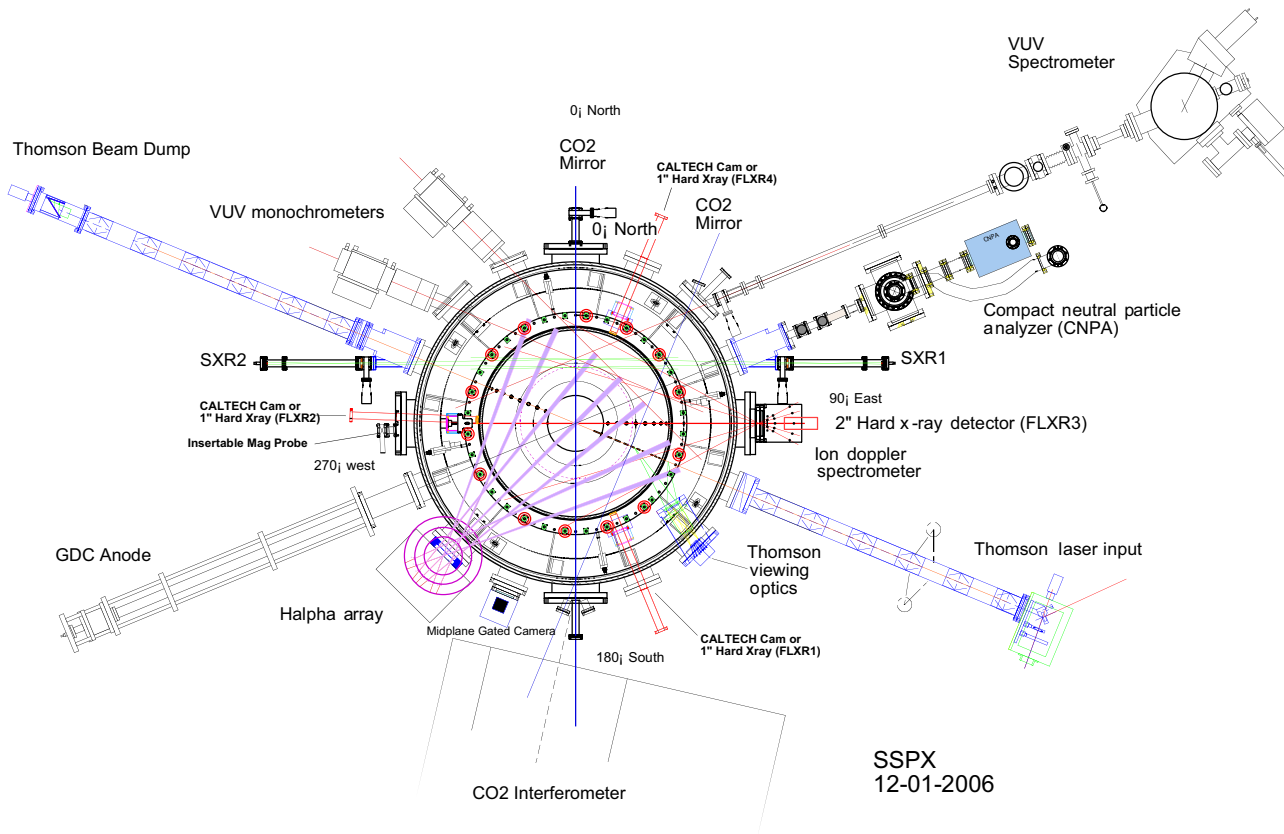


**Figure 3.** Overview of SSPX diagnostics.

poloidal flux in SSPX are in good agreement with resistive-MHD simulations up to a saturation level which is not predicted by the calculations. The role of magnetic fluctuations in the evolution of the plasma is described in section 3.5, and the thermal transport in the core of the spheromak is given in section 3.6. Interestingly, in quiescent regimes (fluctuation levels below 1% of the flux-averaged field) the thermal diffusivity in the core is comparable to that in the tokamak L-mode. Section 3.7 describes experiments and simulations of pulsed, ‘refluxing’ operation in which the plasma is allowed to decay slowly while it has good confinement, followed by a rebuilding of the flux and current before another slow decay period. If the good confinement decay can be extended sufficiently long, this represents a possible mode of operation for future spheromak experiments. In section 3.8, beta limits in a large-aspect ratio ( $\sim 2$ ) spheromak are shown to be in good agreement with the Mercier limit; section 3.9 describes additional physics results including helicity balance and transport studies.

### 3.2. Discharge and operational parameters

As discussed in section 2.6, wall conditioning and impurity control were required to obtain good physics results. Each day of operation started with deposition of titanium on the flux-conserver inner wall interspersed with discharge-cleaning shots. Additional titanium gettering was applied regularly throughout the day to maintain the good vacuum conditions. Power-balance measurements demonstrated that

impurity radiation accounted for as low as 10% of the power appearing as radiation; typical discharges had  $\sim 20\%$  in impurity radiation.

The poloidal bias magnetic field was applied a few seconds before each discharge, allowing eddy currents in the flux conserver to die away. An example of the axisymmetric-field geometry of the spheromak [30] generated by the discharge is shown in figure 4.

At the start of the discharge, hydrogen or other gas was puffed into the coaxial gun at the inward bend of the outer flux-conserver wall. A typical discharge started with a high-current formation phase followed by a lower current-sustainment phase lasting 1–4 ms. An example is shown in figure 5.

As the spheromak current is nearly force free the axisymmetric magnetic profile is approximately determined by  $\nabla \times \mathbf{B} = \lambda(r, z)\mathbf{B}$ , with a radial profile given by  $\lambda(r, z)$ . This leads to the Grad–Shafranov equation; including the effects of pressure gives

$$\Delta^* \psi = -\lambda \int_0^\psi \lambda \, d\psi - \mu_0 r^2 \frac{dp}{d\psi}. \quad (1)$$

Example solutions for  $\lambda(r)$  and  $q(r)$  in the SSPX geometry are given in [23]. Note the existence of the x-point in the bottom of the gun. This leads to a separatrix bounding the spheromak in the flux conserver with the safety factor diverging at the separatrix. As will be seen, the physics of the plasma near the separatrix plays an important role in the spheromak

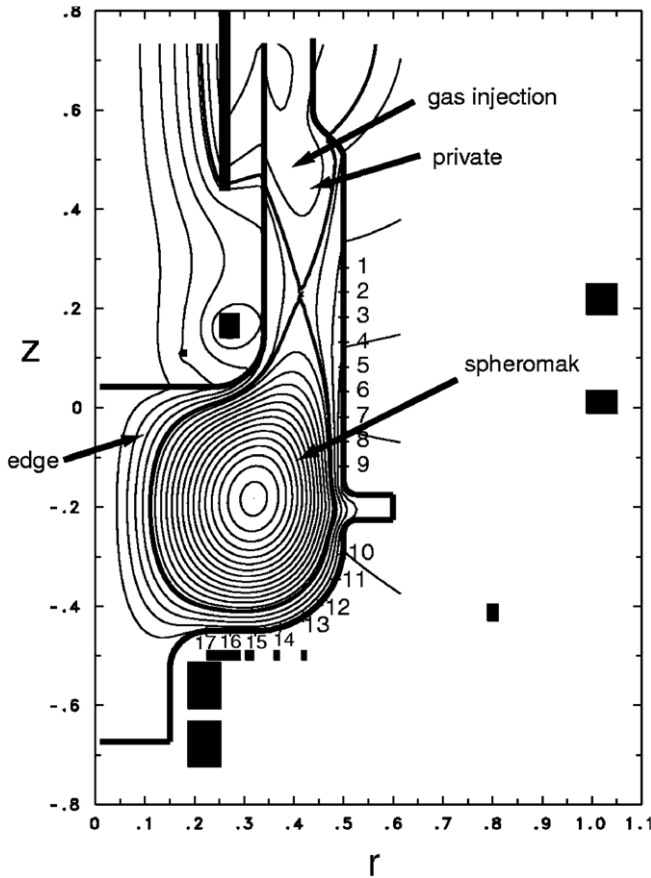


**Figure 4.** Poloidal magnetic flux for an example equilibrium. The flux contours correspond to 0.5 mWb steps. From [30].

stability and formation of closed flux surfaces. If the separatrix contacted the wall forming a limited plasma, high impurity levels usually resulted.

The current from the gun lies outside the separatrix in the mean-field (axisymmetric) approximation and effectively determines the value of  $\lambda(r)$  on the separatrix [23]. In experiments this gives a rough control over the  $q$ -profile. In particular, by keeping this close to the Taylor value (or eigenvalue for  $\nabla \times \mathbf{B} = \lambda_{FC} \mathbf{B}$  with  $\lambda_{FC} = \text{const}$  the lowest eigenvalue for the flux conserver), the safety factor can be kept above 0.5 thereby avoiding a discharge-terminating  $n_\phi = 2$  MHD mode during the sustainment phase. This mode is seen at the end of the discharge [31] and shown in figure 5 when the injected current drops and the  $q = 1/2$  surface enters the plasma at 3.5 ms. CTX also observed discharge-ending modes with  $n_\phi > 1$  [32].

### 3.3. Spheromak formation

Plasma formation in SSPX typically used an initial current pulse with  $\lambda_{\text{gun}} > \lambda_{FC}$ , as seen in figure 5. The high-current discharge generated a plasma which expanded, blowing out of the gun. Photographs using a high-speed camera were used to capture images of the plasma using atomic line radiation. Soon after the ejection they show a sheet forming a coaxial bubble as it leaves the gun with the return current subsequently pinching down into a central column. Resistive-MHD simulations

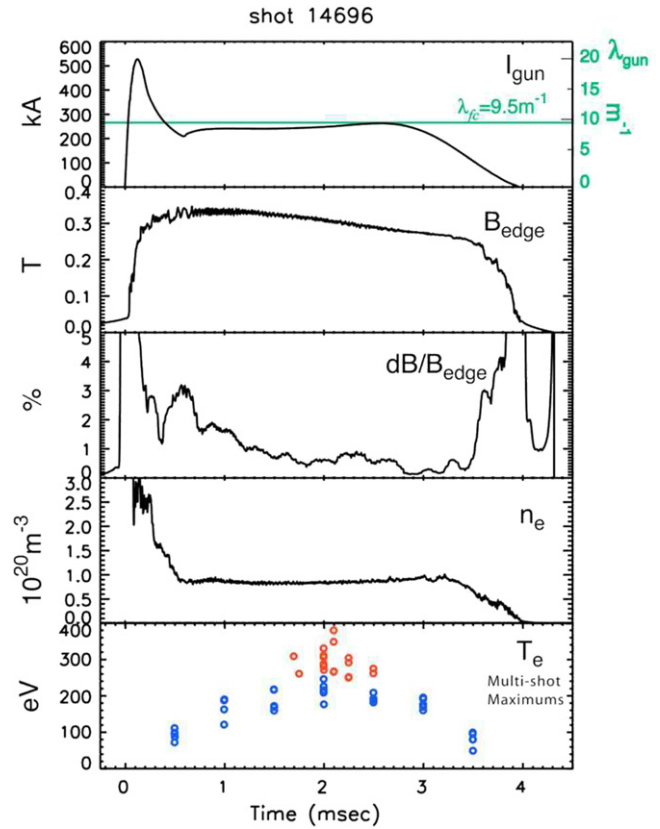


**Figure 5.** Typical discharge timing. Top-to-bottom: injector current ( $\lambda_{\text{gun}} = \mu_0 I_{\text{gun}} / \psi_{\text{gun}}$ ), edge magnetic field at the midplane, fluctuation level, line-averaged density, electron temperature. From [31].

(appendix B) in figure 6 also show the plasma ‘bursting’ from the gun, filling the flux conserver and then pinching about its geometric axis.

Following the pinching, the central column goes unstable to a MHD mode with toroidal mode number  $n_\phi = 1$ , as seen in other coaxially injected spheromaks [7–9, 12, 13]. Probe measurements in the coaxial gun region show that the  $n_\phi = 1$  structure has a large amplitude there and that there are torques on the plasma due to cross-field currents associated with the mode [33]. This mode grows until an initial reconnection event occurs, converting some of the injected toroidal flux into poloidal flux and forming the spheromak magnetic geometry [34]. An example of photographic images of the sinking of the central column during the formation phase in SSPX is given in figure 7. These images were compared with visualizations using VisIt graphics software<sup>7</sup> produced from a NIMROD simulation shown in figures 8–10. An insertable probe was used to produce measurements of the poloidal and toroidal magnetic field (figure 6), and provided quantitative support for the physics discussed below [35]. The current column down the geometric axis pinches, shifts or tilts, and then kinks during formation in almost all strongly driven ( $\lambda_{\text{gun}} \gg \lambda_{FC}$ ) SSPX discharges as shown in photographs in figure 7 and

<sup>7</sup> VisIt is a visualization program for visualizing numerical simulation data on meshes. VisIt was developed by the Department of Energy (DOE) Advanced Simulation and Computing Initiative (ASCI) to visualize and analyze the results of terascale simulations <http://www.llnl.gov/visit/>.



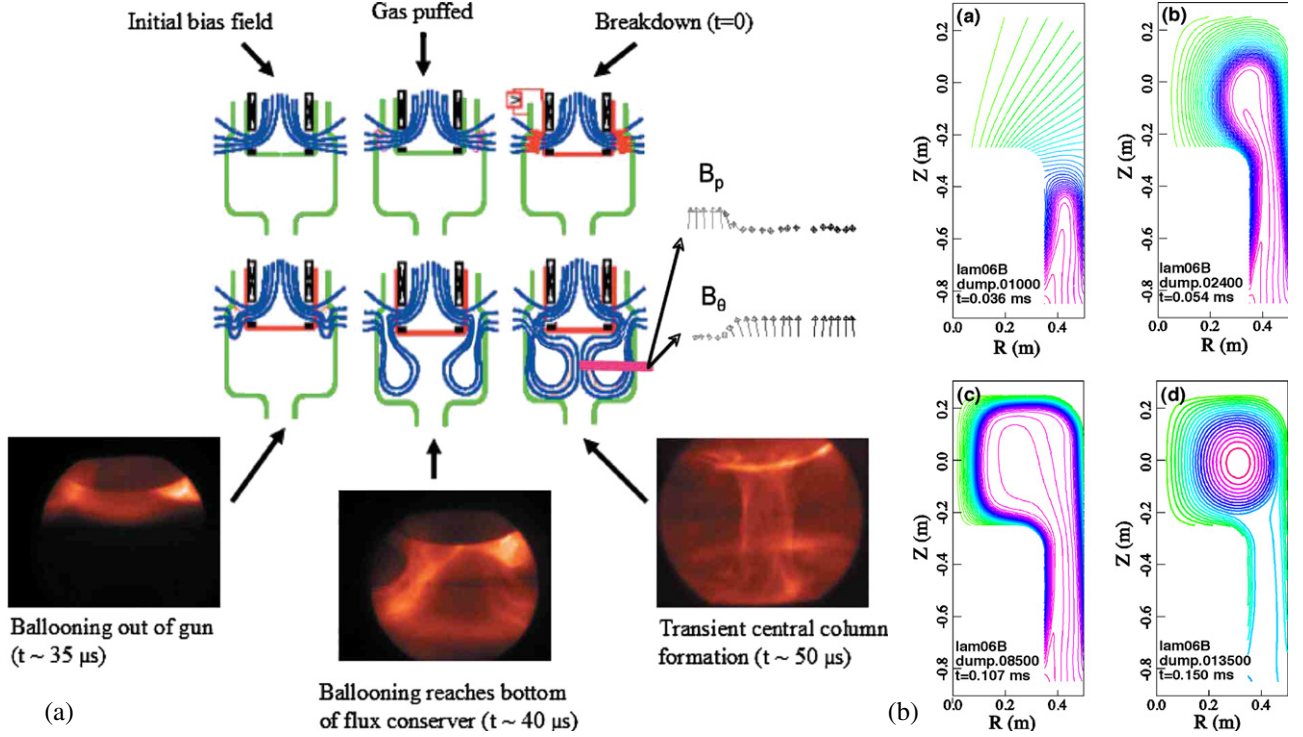


**Figure 6.** Plasma formation. (a) Photographs showing ejection and formation of the central column. Also shown are magnetic-probe measurements of the poloidal and toroidal magnetic field. From [36]. (b) Toroidally average poloidal flux contours in NIMROD simulation *lam06b* (from a series scanning  $\lambda_{\text{gun}}$ ) at the times shown in the figures. Note that in the experiment the gun is at the top whereas in simulations it is at the bottom.

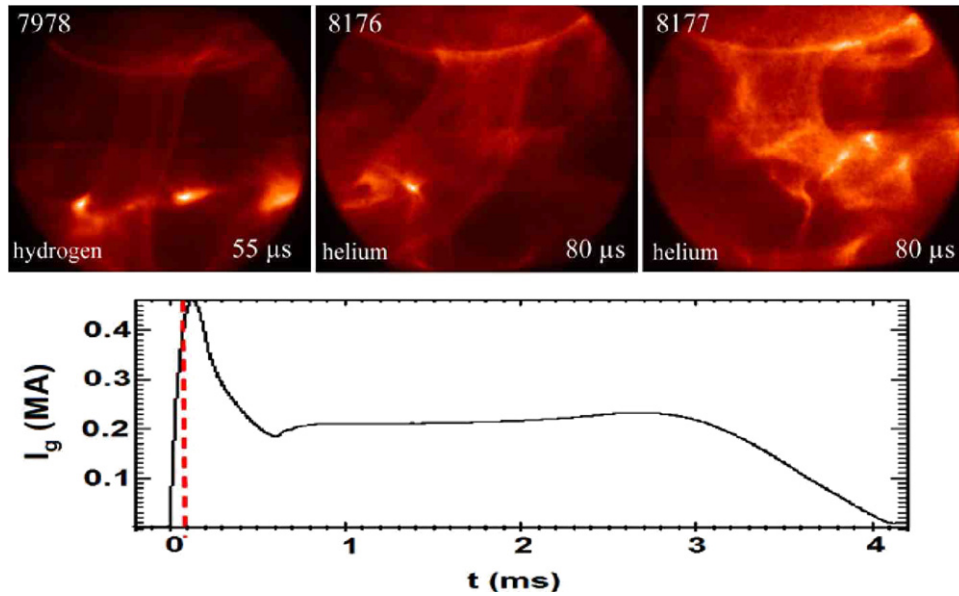


**Figure 7.** Top: photographic images of SSPX discharges showing kinks in the central column during formation in hydrogen and helium. Bottom: gun current time dependence showing the formation period with the dashed line at  $80 \mu\text{s}$ . From [34].

in more detail in [35, 36]. In the examples considered here  $\lambda_{\text{gun}} \approx 18 \text{ m}^{-1}$  for the peak gun current, and  $\lambda_{\text{FC}} \approx 10 \text{ m}^{-1}$ .

In figure 8 we plot constant  $\lambda = 20 \text{ m}^{-1}$  surfaces at four times from the NIMROD simulation with  $n_\phi = 0, 1, \dots, 5$  toroidal Fourier modes. Figure 9 has images of constant-temperature surfaces at several times spanning the formation event. Because of the high thermal conduction parallel to the magnetic field, temperature evolution is a sensitive

indicator of energy confinement and its relation to the magnetic configuration. We observe in figures 8 and 9 the growing displacement, twisting and kinking of the current column and the beginning of the detachment of part of the kink which contributes to the formation of the toroidal current ring required for establishing the spheromak poloidal magnetic field. The kinking of the column in the simulation (figure 9) resembles the photographic images of SSPX in figure 7 and in [34–37]. At

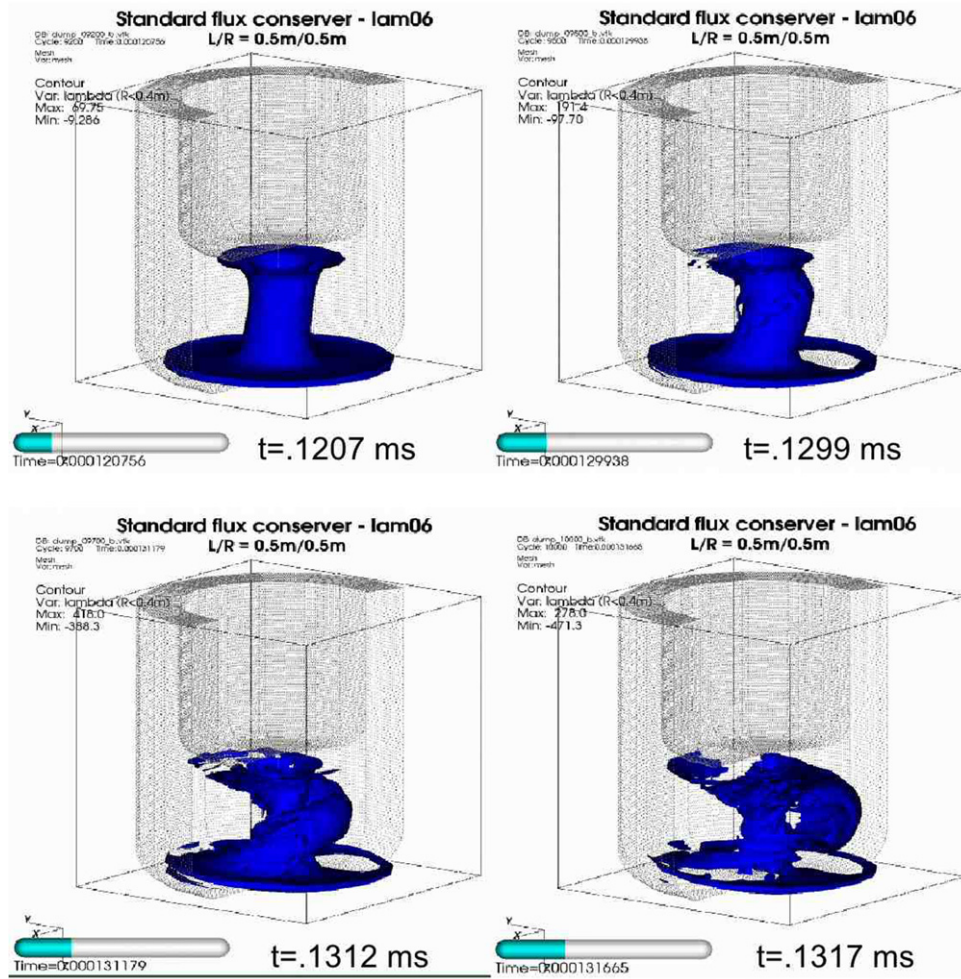


**Figure 8.** Constant  $\lambda = 20 \text{ m}^{-1}$  surfaces at four times:  $t = 0.120756$ ,  $0.129938$ ,  $0.131179$ , and  $0.131665 \text{ ms}$  in the *lam06b* NIMROD simulation. From [34].

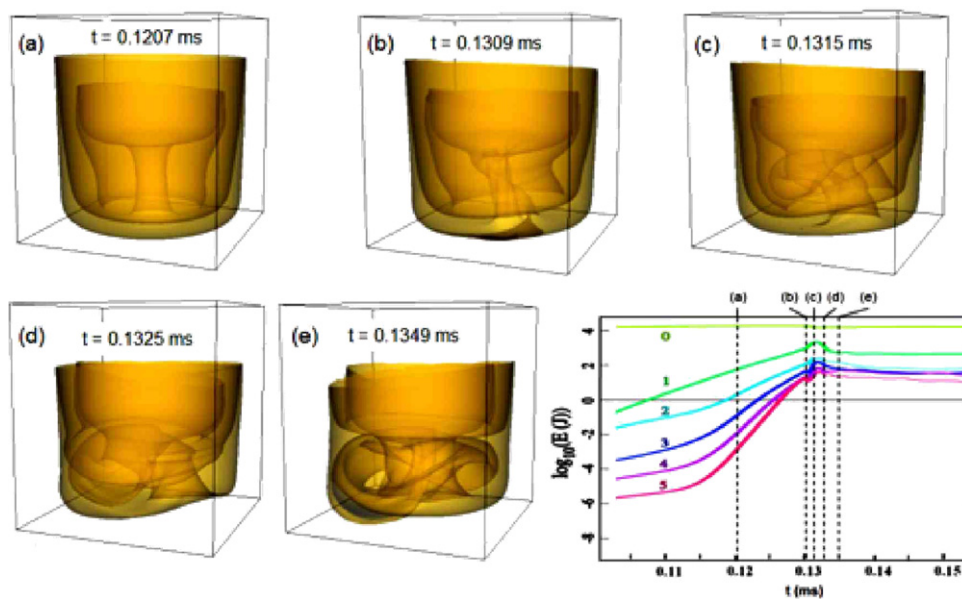


**Figure 9.** Constant-temperature surfaces at five times during formation in the NIMROD simulation. The lower right inset corresponds to the toroidal magnetic energy integrated over volume throughout this period and separated by toroidal mode number. From [34].

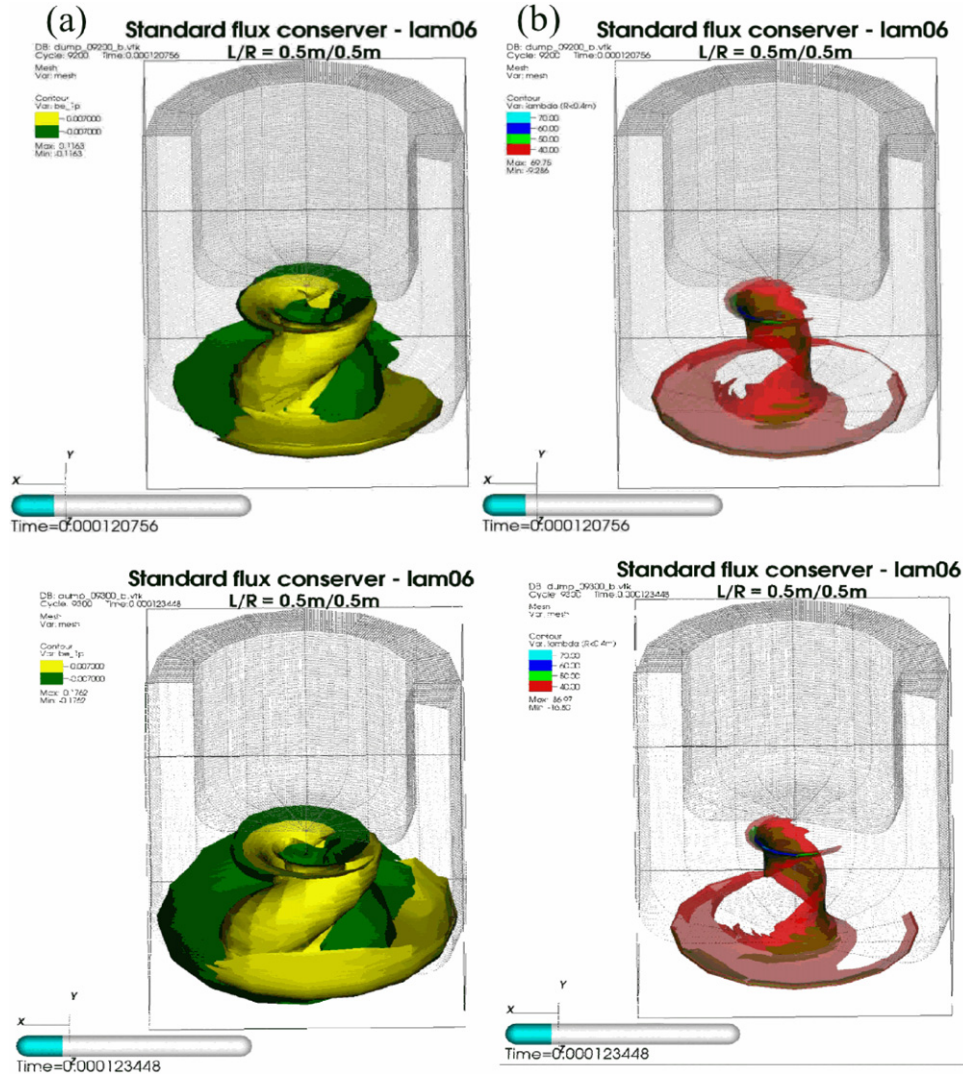


**Figure 10.** (a) Constant  $B_\phi(n_\phi = 1) = \pm 0.007$  T surfaces in yellow and green, and (b) four constant  $\lambda = 40, 50, 60$  and  $70 \text{ m}^{-1}$  surfaces at  $t = 0.120756$  and  $0.123448$  ms. From [34].

the onset of the spheromak formation event ( $t \sim 0.13$  ms), the maximum temperature in the volume is observed to rapidly decrease. When a simulation was performed with only  $n_\phi = 0$  and 1 toroidal modes, qualitatively similar results were observed; however, the spheromak formation event occurred later in time, and the range in values of  $\lambda$  was narrower suggesting that the current filaments were somewhat weaker.

In figure 10 we reproduce a plot of the constant  $B_\phi(n_\phi = 1) = \pm 0.007$  T surfaces and four constant  $\lambda$  surfaces before the major reconnection event. The visualizations show the pinching, tilting and kinking of the current channel, and the sequence of events leading to the reconnection event forming the spheromak. An analytical calculation of the linear kink instability of the central current column also appeared in [34] and captures the main features of the instability seen in the simulations.

Time traces of injector current, voltage and magnetic energy (decomposed into toroidal Fourier modes) from the simulation of SSPX are shown in figure 11; and poloidal contour plots of the toroidally averaged poloidal magnetic flux are shown in figure 6(b) at the four times indicated in figure 9.

A significant voltage spike due to inductive effects occurs at  $t \sim 0.13$  ms in the NIMROD simulation (figure 11(b)) accompanying the formation of the mean-field spheromak (evidenced in the toroidally-averaged poloidal flux contours in figure 6(b)); the spike is also observed in the experiment [38, 39]. The injector current has already peaked, and the growth of the  $n_\phi = 1$  kink mode terminates at  $t \sim 0.13$  ms when the formation event occurs. A linearly growing  $n_\phi = 1$  kink mode is observed in figure 11(c). There are growing harmonics of the  $n_\phi = 1$  mode whose growth rates  $\gamma_n$  scale almost linearly with respect to the toroidal mode number  $n_\phi$  compared with the observed growth rate of the  $n_\phi = 1$  mode. Sovinec *et al* [40] also observed a linear scaling  $\gamma_n = n\gamma_1$  in earlier NIMROD simulations using a different model for driving the spheromak based on programming the gun voltage instead of the gun current used here. The nearly linear scaling of the growth rates of the harmonics suggests that the harmonics are nonlinearly driven and that they inherit their growth from the  $n_\phi = 1$  mode.

When the reconnection event occurs at  $t \sim 0.13$  ms, the  $n_\phi = 0$  magnetic energy decreases; and there is a



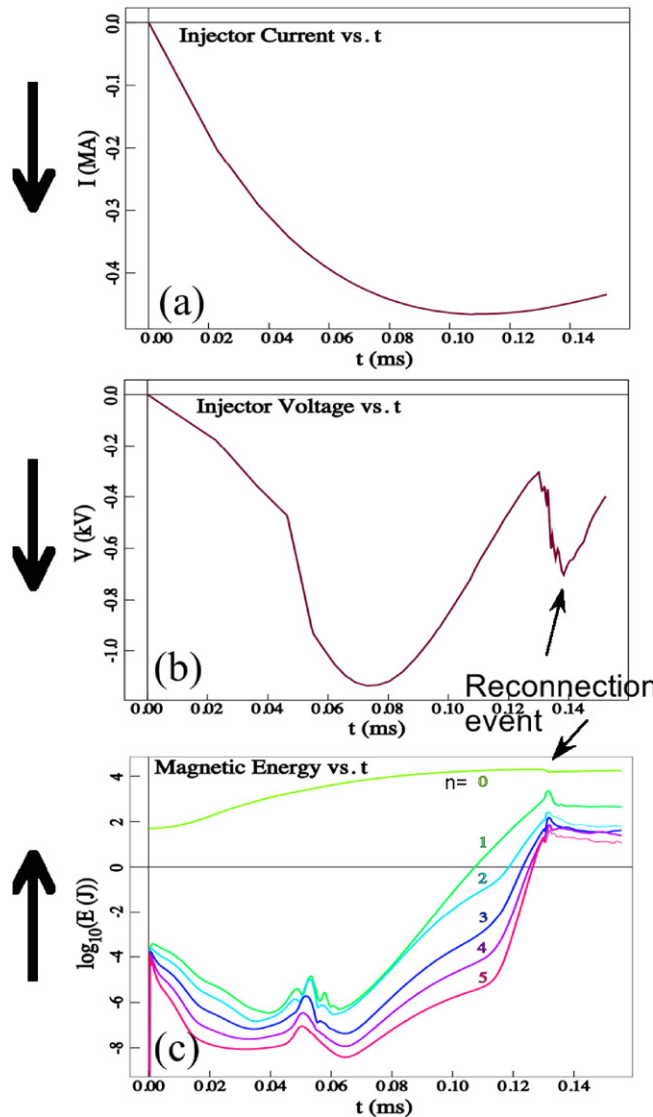


**Figure 11.** NIMROD simulation showing time traces of (a) injector current, (b) injector voltage and (c) toroidal magnetic energy integrated over volume. From [34].

concomitant increase in kinetic energy at all  $n_\phi$  values and in the nonzero- $n_\phi$  magnetic energy. In the *lam06b* simulation the reconnection event occurs when the  $n_\phi = 1$  component of the magnetic energy averaged over the volume is  $\sim 10\%$  of the  $n_\phi = 0$  magnetic energy. Assessment of energy balance in the simulations showed that there is substantial energy flow from the axisymmetric magnetic configuration into non-axisymmetric magnetic perturbations and kinetic energy during reconnection, and heat flow to the walls along open-field lines. The kinetic energy perturbation and the finite- $n_\phi$  magnetic energy then quickly relax, and the  $n_\phi = 0$  magnetic energy partly recovers. The evolution of the kinking central column pictured in figures 8–10 correlates with the evolution of the magnetic and kinetic energies in the system. The  $n_\phi = 1$  kink in the current channel and the associated magnetic field perturbations blow out to larger radius during the reconnection event and form a detached current ring. The amplitudes of the magnetic perturbations increase briefly in time, almost explosively, as this happens.

Thus, the results from a NIMROD nonlinear, resistive-MHD simulation of spheromak formation physics compare well with photographs of the SSPX plasma and measurements made with the insertable magnetic probe [34]. The growth of an  $n_\phi = 1$  mode is a dominant feature. The column mode shifts and twists the central current channel creating a toroidal component of the current, and the twisting kink thus creates poloidal magnetic flux as the helicity in the system grows. The growth of the kink terminates in a fast event in which there is reconnection of the current and magnetic flux into a spheromak configuration. The  $n_\phi = 1$  mode is always observed during spheromak formation in SSPX with strong drive and in three-dimensional simulations of such discharges in SSPX with NIMROD [38, 39, 41, 42]. NIMROD simulations constrained to be axisymmetric form spheromaks with very little positive poloidal magnetic flux inside the separatrix [38]. The phenomenological model of the  $n_\phi = 1$  column mode presented in [34] captures the main features of the instability seen in the simulations.

### 3.4. Current and flux amplification

Following the initial reconnection event, the plasma continues to build, increasing the poloidal flux by additional reconnections and reaching an eventual saturation which is weakly dependent on the bias magnetic flux configuration and the time history of the gun current. Experimental results were summarized in [43]. Figure 12 shows the achieved values of  $B_p/I_{\text{gun}}$ , with  $B_p$  the peak value of the poloidal field at the flux conserver for several current time histories. A peak  $B_p/I_{\text{gun}}$  was found for values of  $\lambda_{\text{gun}}$  slightly above  $10 \text{ m}^{-1}$  as seen in figure 13.

The voltage spikes during injection, as seen in figure 14, are found to result from reconnection events [44]<sup>8</sup> which continue as long as  $\lambda_{\text{gun}} > \lambda_{\text{FC}}$ . At each event, the simulation shows the flux surfaces opening as in figure 15; the high parallel thermal conductivity along field lines to the walls drops the electron temperature (figure 16). Although surfaces may close following reconnection allowing the temperature to rise, the time between events is short enough that the peak electron temperature is limited to about 100 eV or less.

The current density in the plasma, as measured by  $\lambda$ , shows considerable structure, especially near the x-point as seen in figure 17. Interestingly, fundamental research in magnetic reconnection since this work has found that fast reconnection in the resistive-MHD approximation occurs when plasmoids (tearing-generated ‘flux-ropes’) are generated at the reconnection layer [45]. The reconnection rates are rapid and much closer to those with Hall physics than found without the plasmoids. Future research is needed to determine whether such an effect is occurring in the three-dimensional simulations for the spheromak.

The buildup reaches a flux amplification which is proportional to  $\lambda_{\text{gun}} - \lambda_{\text{FC}}$  [46–48]. The agreement of the simulations with experiment is shown in figures 18 and 19 and is excellent up to about  $\lambda_{\text{gun}} = 14 \text{ m}^{-1}$ . At higher values

<sup>8</sup> An instability at the cathode surface may also contribute to voltage spikes in the experiment. See [44].



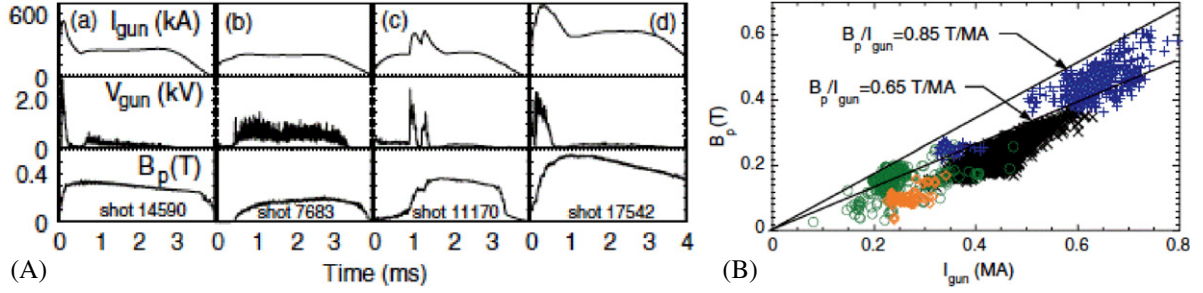


**Figure 12.** (A) Time history of gun current ( $I_{\text{gun}}$ ), gun voltage ( $V_{\text{gun}}$ ) and edge poloidal field for (a) standard formation followed by sustainment, (b) slowly building, (c) double pulse and (d) extended formation discharges. (B) Peak edge poloidal field versus peak gun current for standard formation (black x's), slowly building (green circles), double pulse (orange diamonds) and extended formation (blue crosses) discharges. From [43].

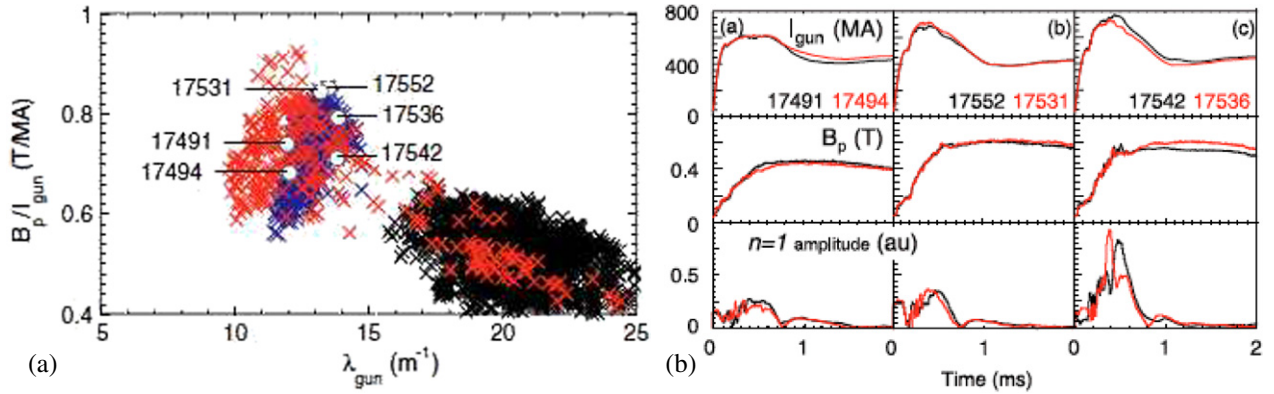


**Figure 13.** (a) Peak edge poloidal field buildup parameter ( $B_p/I_{\text{gun}}$ ) versus  $\lambda_{\text{gun}}$  for standard formation (black), extended formation (blue) and extended formation with extended flux-conserver (red) discharges. Time histories of shots with white circles are shown in (b). (b) Time histories of gun current ( $I_{\text{gun}}$ ), edge poloidal field ( $B_p$ ) and  $n = 1$  mode amplitude for discharges with (a)  $I_{\text{gun}} < I_{\text{crit}}$ , (b)  $I_{\text{gun}} = I_{\text{crit}}$  and (c)  $I_{\text{gun}} > I_{\text{crit}}$ . Here,  $I_{\text{crit}} = 2\pi\psi_{\text{gun}}/\mu_0 h$  with  $h$  the spheromak height (0.5 m). From [43].

of  $\lambda_{\text{gun}}$ , however, the buildup in the experiment saturates [49] as seen in figures 13(a) and 18(b), whereas the simulation continues to increase as shown by the solid lines in figures 18. The reason for the saturation is not well understood but apparently lies outside the physics of single-fluid, non-Hall resistive MHD.

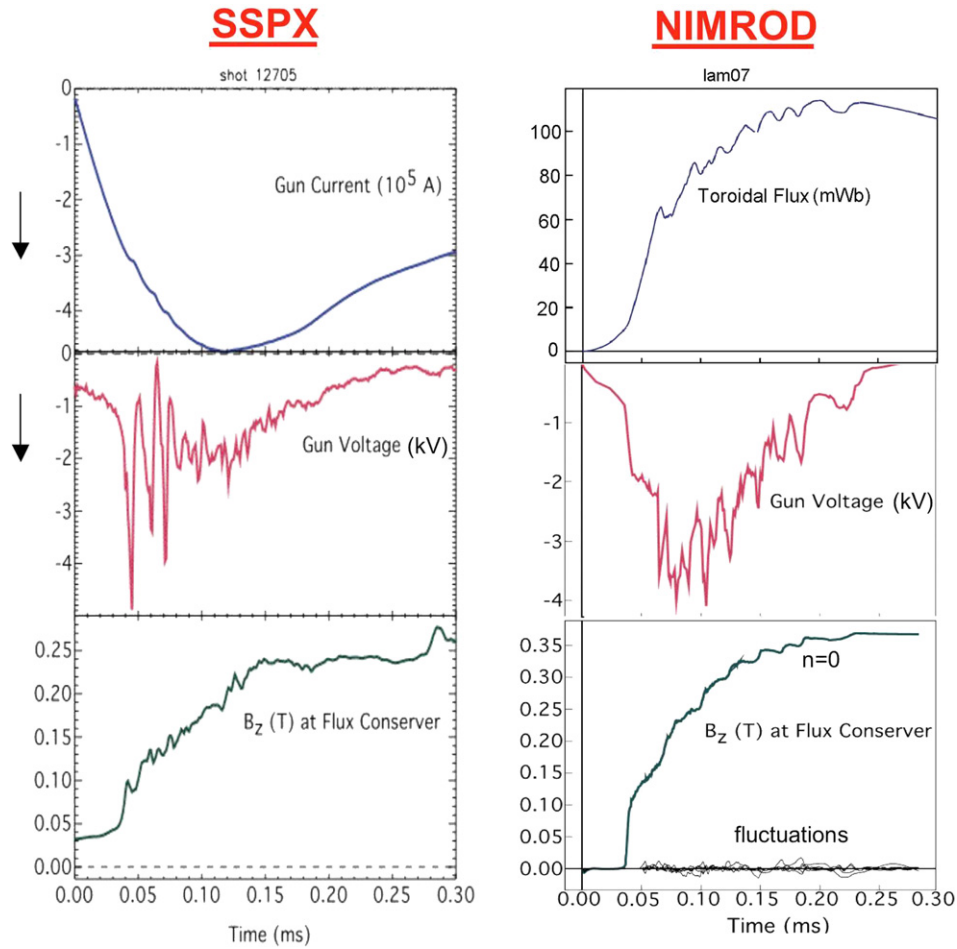
### 3.5. Role of fluctuations in spheromak evolution

Following the generation of the spheromak configuration, the current drive could be removed by reducing the gun current sufficiently that  $\lambda_{\text{gun}} < \lambda_{\text{FC}}$ . The plasma current and magnetic field slowly decay with the safety-factor profile evolving on the same timescale. It is known from theory that the safety-factor profile must pass through  $\lambda_{\text{FC}}$  [50]. As a result, during its evolution with the edge value about  $\lambda_{\text{FC}}$ , it will typically pass through a relatively flat profile at which time the plasma is typically relatively quiescent with magnetic fluctuation levels  $\sim 1\%$  or less. Flux surfaces closed over much of the volume, providing good confinement and strong electron heating, reaching a temperature as high as 500 eV. Energy confinement in the plasma core became high, as will be discussed in section 3.6.

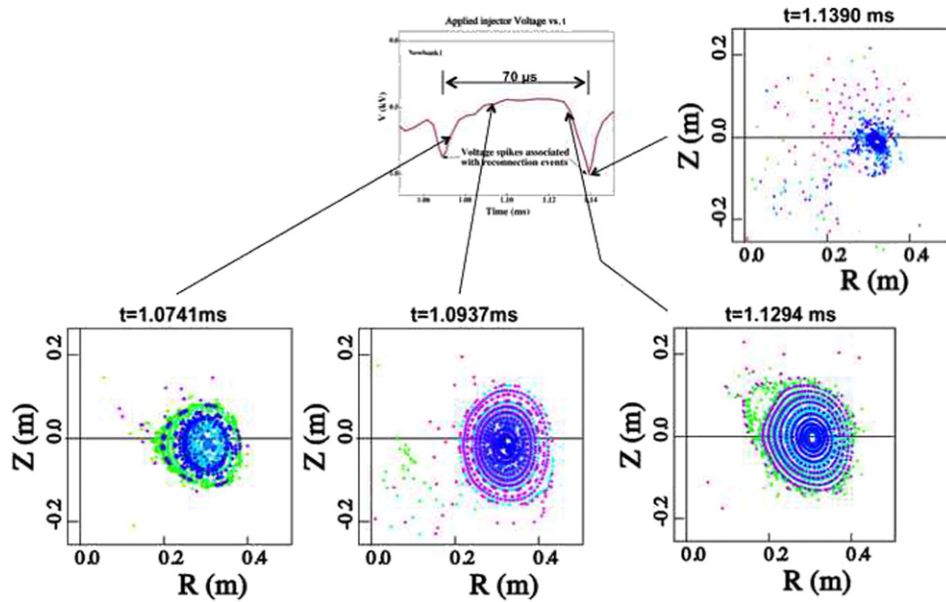
As noted in section 2.3, one of the features of SSPX was the ability to adjust the geometry of the vacuum (bias) poloidal magnetic flux. In experiments with low fluctuation levels,

the vacuum configuration was adjusted such that substantial vacuum flux left the gun, allowing operation at  $\lambda_{\text{gun}}$  below the ‘bubble-burst’ condition where  $\lambda_{\text{gun}} = \pi/\Delta \approx 20 \text{ m}^{-1}$ , with  $\Delta$  the gun gap width. Operation with  $\lambda_{\text{gun}} \approx \lambda_{\text{FC}}$  yielded an early result of the experiment [51] with the results seen in figure 20(a); the resulting quiescent period is shaded. Figure 20(b) shows the configuration used in the experiments in figure 20(a). If the vacuum flux were mostly confined to within the gun, the low  $\lambda_{\text{gun}}$  and quiescent state could not be achieved.

Resistive-MHD simulations of this shot [38, 41] were in good agreement with the experiment results, including magnetic fluctuation levels and temperature. Figures 21 and 22 show the comparison from [38]. The buildup in the  $n_\phi = 0$  poloidal magnetic field in the simulation tracked the experiment until  $t \sim 0.3$  ms when there was an error in the current-drive model (the spike and downward correction in the gun current), which resulted in an accompanying spike and correction in the gun voltage and a steep decrease in the magnetic field. The later fluctuation behavior was modified only slightly. During the early part of the formation ( $t < 0.3$  ms), the simulation sees the  $n_\phi = 1$  toroidal mode at relative amplitudes similar to the experiment. After 0.5 ms the fluctuations begin to relax in the simulations and in the SSPX shot. At around 4 ms  $n_\phi = 2$  fluctuations emerge in both the experiment and the simulation as the spheromak plasma dies.



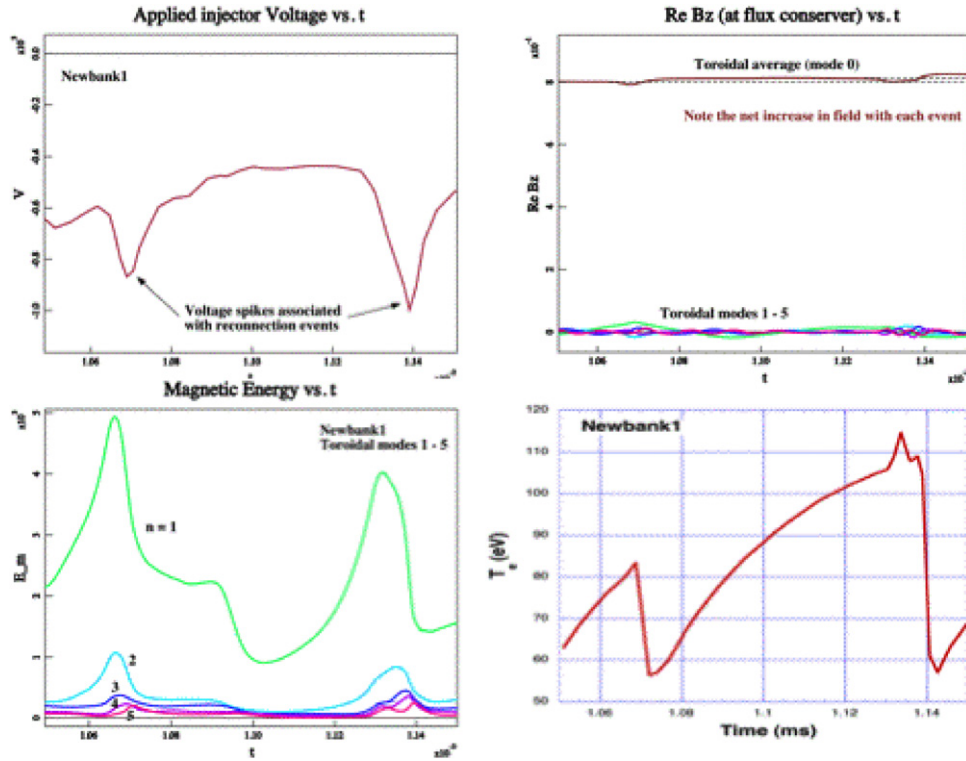
**Figure 14.** Comparison of experimental and simulated buildup. From [39].



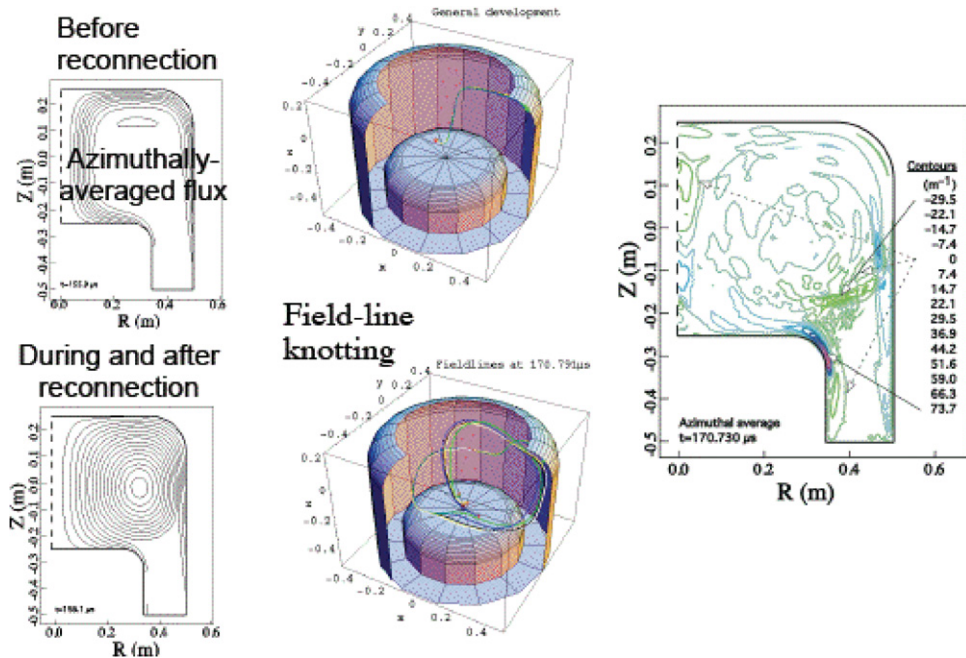
**Figure 15.** Surfaces open at the reconnection event and ‘heal’ thereafter’.

Figure 21 shows similar fluctuation data from SSPX discharge shot #12560 and a simulation. It also shows the time history of the peak electron temperature in *lam06* and as measured by Thomson scattering in SSPX shot #12560.

The NIMROD simulation used a single-fluid model with  $T_e = T_i$  assumed. If the ions were in fact colder than the electrons, this would imply that the electron temperature might have to be higher to give the same total pressure as calculated in



**Figure 16.** Effects of voltage spikes (upper-left) due to reconnection events. Upper-right: increase in toroidally averaged, poloidal field at each event. Lower left: energy in the MHD modes driven by the current column from the gun. Lower right:  $T_e$  changes associated with each event. From [46].



**Figure 17.** Toroidally averaged poloidal flux, magnetic field lines, and  $\lambda$  contours showing topology change in the magnetic field attributed to reconnection. Reconnection is generated by current sheets with negative  $\lambda$ , which are strongest near the x-point of the mean-field spheromak. From [39].

NIMROD. For the 120 eV peak electron temperature, the peak electron  $\beta_e \sim 4\%$  in the simulation. A magnetic field-line plot (figure 22) is highly revealing: the magnetic flux surfaces in the core of the spheromak are closed. Magnetic islands link the temperatures from one side of an island to the other and

locally flatten the temperature profile. Closed nested magnetic surfaces are surrounded by confined magnetic field lines that are chaotic, and the field lines are open surrounding the confined region. The transition from stochastic confined field lines to open-field lines is accompanied by a steep drop in the



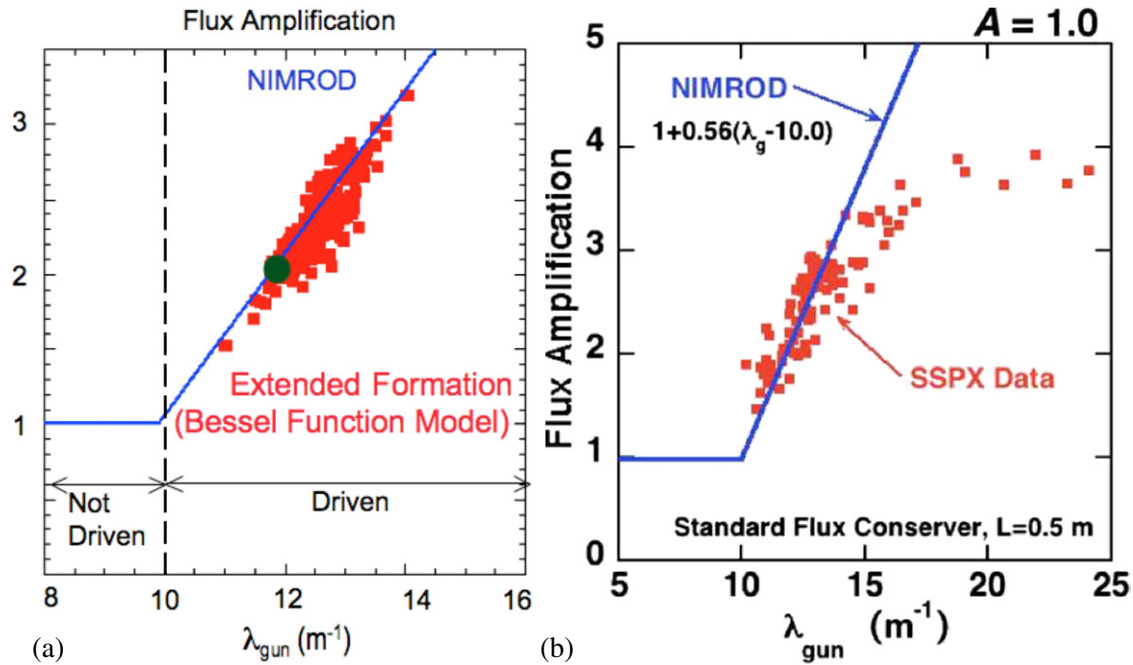


**Figure 18.** Poloidal flux amplification in SSPX. The square points are from the experiment. (a) Comparison of a Bessel function model (red points) for flux amplification in the experiment and NIMROD (blue line) for  $\lambda_{\text{gun}} < 14 \text{ m}^{-1}$ . The data point analyzed in figure 19 is shown in green. From [48]. (b) Flux amplification showing saturation in the experiment for  $\lambda_{\text{gun}} > 14 \text{ m}^{-1}$ . From [49].

electron temperature which tracks the experimental Thomson-scattering data well. Good energy confinement depends strongly on the presence of magnetic surfaces and the quality of the field lines. Poor confinement arises where the field lines become chaotic as the separatrix of the  $n_\phi = 0$  poloidal flux is approached. Later work [52] demonstrated quantitatively that the divergence of the safety factor as it approaches the separatrix allows excitation of multiple MHD modes which cause this behavior. This results in an effective reduction of the minor radius of the spheromak confinement region, with the electron temperature profile narrowed accordingly. It also found that during the decay the  $\lambda$ -profile eventually becomes non-monotonic due to the spatially varying plasma resistivity, resulting in the formation of unstable regions and magnetic islands which limit energy confinement.

Additional NIMROD simulations modeling SSPX are reported in [42]. This work shows good matching of the current–voltage characteristics between the experiment and simulation. This study also addresses the dependence of the simulation results on some of the numerical parameters in NIMROD as well as whether the NIMROD simulations could recover the peak electron temperatures observed in the experiment. The NIMROD simulations tended to underpredict the temperatures observed in the experiment, e.g. 20–40% lower than some SSPX data. The simulations were much better in matching the magnetics observed in the experiment than the electron temperatures, which was attributed in part to the very large parallel thermal conduction.

### 3.6. Fluctuations and thermal transport

The experimental results discussed in section 3.5 were extended and optimized [31]. Energy confinement

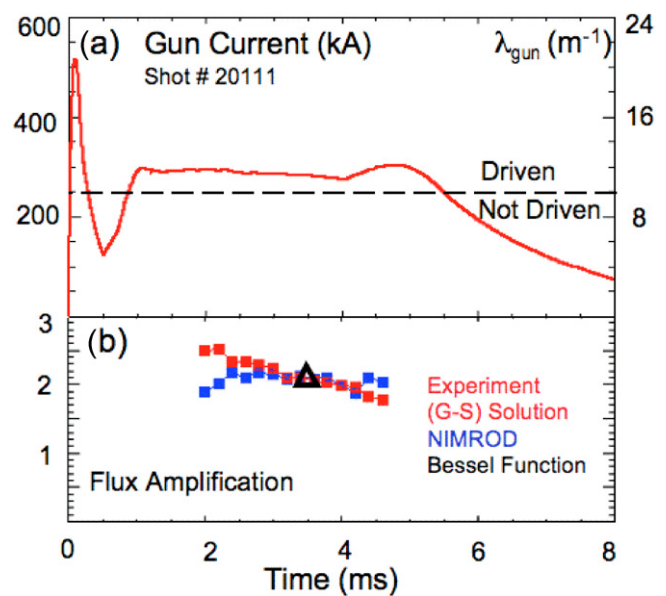


**Figure 19.** Time-dependent flux amplification reproduced by NIMROD. (a) Constant current above flux-conserver eigenvalue,  $\lambda = 9.9 \text{ m}^{-1}$ . (b) Flux amplification from equilibrium reconstruction (red) versus NIMROD (blue) and a single point analyzed with a Bessel function model. From [48].

was increased significantly. High bias poloidal fluxes (50–100 mWb) and gun currents resulted in electron temperatures as high as 0.5 keV [43]. The thermal conductivity in the core plasma was measured to be as low as  $1 \text{ m}^2 \text{ s}^{-1}$ .

Electron temperature measurements as a function of  $\lambda_{\text{gun}} \approx \lambda_{\text{FC}}$  found an optimum slightly below  $\lambda_{\text{gun}} = 10 \text{ m}^{-1}$



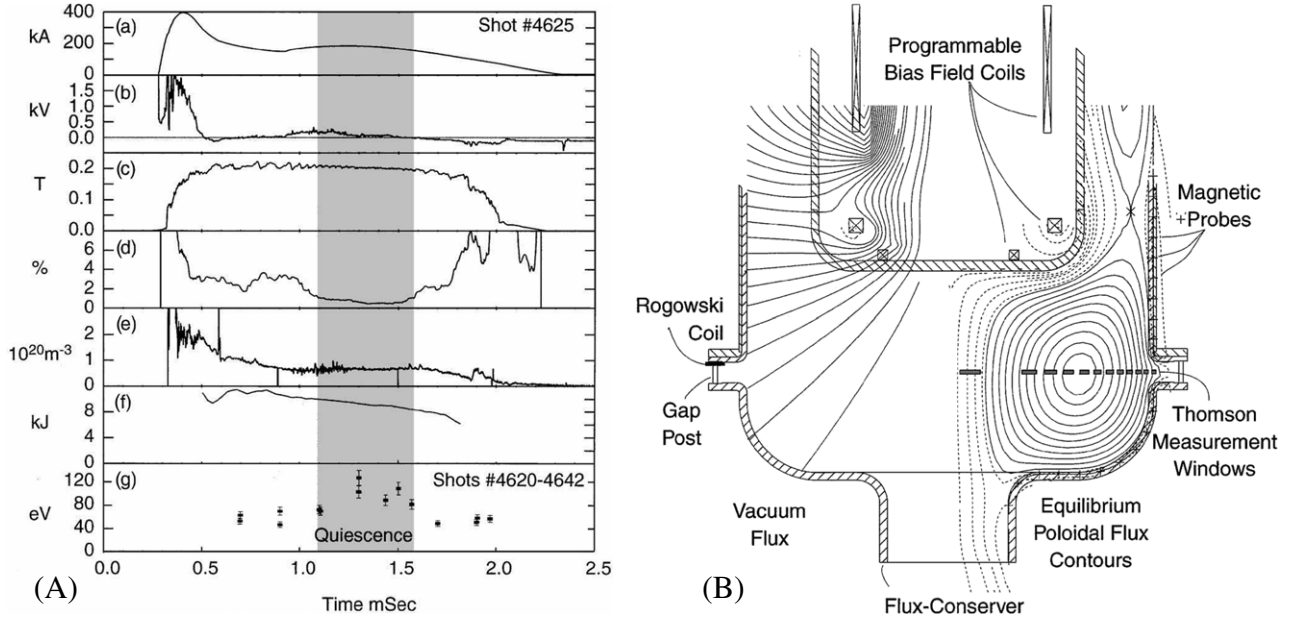


**Figure 20.** (A) Time histories for SSPX key parameters: (a) injector current, (b) injector voltage, (c) edge poloidal field, (d) rms magnetic field fluctuation level at the wall, (e) chord-averaged electron density, (f) magnetic field energy and (g) central electron temperature,  $T_e$ . (B) Vacuum poloidal magnetic flux (left) and spheromak equilibrium flux (right). From [51].

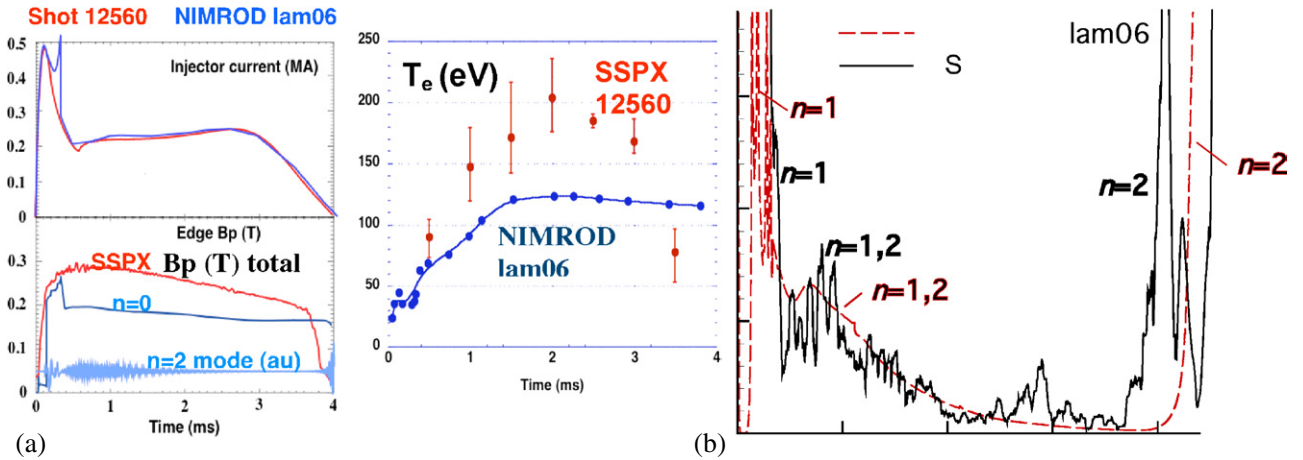


**Figure 21.** (a) NIMROD simulation *lam06b* showing time traces of injector current, edge poloidal field and electron temperature. (b) Time histories of the edge-probe poloidal magnetic field fluctuation data from SSPX discharge shot #12560 and simulation *lam06*. From [41].

as seen in figure 23(a) rather than above this as found for  $B_p/I_{\text{gun}}$  in figure 13. The temperature profile, figure 23(b), was considerably broader than in the initial studies, although thermal conductivity near the edge still was high compared with that in the core.

Low fluctuation levels were highly correlated with the  $q$ -profile, with the  $n_\phi = 2$  and 3 modes quiescent at the high-confinement  $\lambda_{\text{edge}}$  region around the peak-temperature value; the results are given in figure 24. Note that the electron temperature is highly peaked in the stability zone and that the temperature is sensitive to the gun current. This allowed a determination of the scaling of confinement as a function of flux (minor radius) by balancing thermal conductivity at each mean-field flux surface and the internal Ohmic heating within the surface. The experimental electron thermal conductivity

used here is thus defined by

$$\chi_e(\psi) = \frac{\int_0^\psi \eta_{\text{sp}} j^2 \left( \frac{d\text{vol}}{d\psi} \right) d\psi}{\text{Area}(\psi) \frac{d\psi}{dr} n_e e \frac{dT_e}{d\psi}}. \quad (2)$$

The calculation assumes steady state (data are taken at the peak in  $T_e$  versus time when  $dT_e/dt \sim 0$ ), Ohmic heating is the only electron heating source, ion–electron energy exchange is zero ( $T_i = T_e$ ), no radiation heat loss ( $P_{\text{rad}} = 0$ ), and uses a temperature-dependent Spitzer resistivity  $\eta_{\text{sp}}$  with  $Z_{\text{eff}} = 2.3$ .

The above estimate does not include effects of coupling to ions if  $T_e \neq T_i$  as the available diagnostics did not measure the ion temperature in this regime. Hot ions have been observed

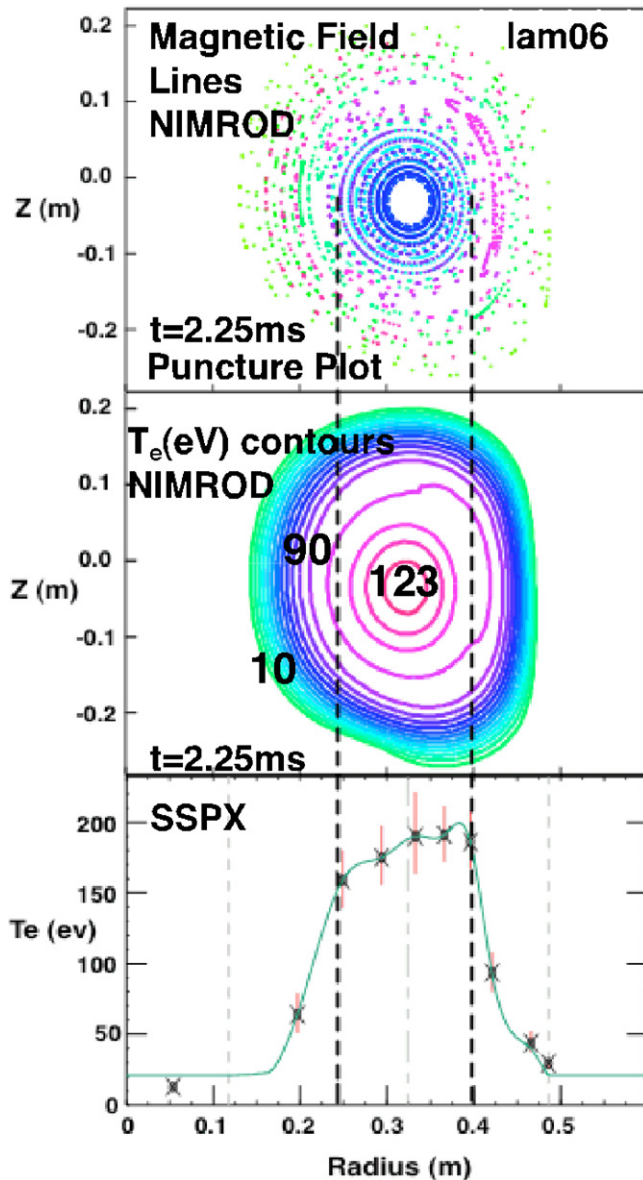


**Figure 22.** Magnetic field-line puncture plot at a reference toroidal angle and the corresponding  $T_e$  contours from simulation *lam06*, and the spatial profile of  $T_e$  from SSPX shot 12560. From [38].

consistently in spheromaks during formation and reconnection [53] and ion heating by fluctuations may play a large role in the initial heat-up of the spheromak after formation [54]. Conversely, the ions will cool at low fluctuation levels due to charge exchange with background neutrals, although this effect should be weak in the spheromak core. Previous ion-Doppler spectrometry measurements of impurity ion temperatures on SSPX [55] have shown  $T_i > T_e$  soon after formation and  $T_e \sim T_i$  during the quiescent phase but the uncertainties in these measurements have remained large due to low signal amplitudes. Charge-exchange measurements are consistent with this result [56]. Indeed, later measurements on a multipulsing discharge [48] showed that the two temperatures roughly tracked one another. If  $T_i = T_e$  the ‘experimental’ thermal conductivity includes an ion contribution in the denominator which depends on  $Z_{\text{eff}}$  and the ion species’

densities. However, these are not well known. Further, at high temperatures the strengths of partially ionized atomic emissions from the core are too low to measure, and there are too few neutrals from the plasma core to determine central ion temperatures with the available diagnostics, so the value of the ion correction is highly uncertain.

Profiles from a set of discharges at 350 eV in the ‘stable’ zone are shown in figure 25. Profile calculations were carried out as a function of electron temperature. The thermal conductivity in the core of the spheromak is plotted in figure 26. Inside  $r/a \sim 0.3$  the average value of  $\chi_e$  is  $< 10 \text{ m}^2 \text{ s}^{-1}$  for  $T_e > 200 \text{ eV}$ . This low value is considered to be characteristic of the intrinsic value for confinement in a spheromak with good electron surfaces.

### 3.7. Sustainment and multiple pulse operation

CHI in SSPX and supporting resistive-MHD simulations were unable to maintain high temperatures ( $> 100 \text{ eV}$ ) while sustaining the current in spheromaks. As in formation, the voltage pulses during sustainment were identified by the simulations as magnetic reconnection events which convert injected toroidal magnetic flux into poloidal flux, generating and maintaining a spheromak mean-field ( $n_\phi = 0$ ) configuration. The reconnection events opened magnetic surfaces, allowing helicity to cross the mean-field surfaces and drive the toroidal current generating the poloidal field. The open surfaces, however, resulted in a high thermal conductivity along field lines to the wall thereby keeping the time-averaged electron temperature low. This result is consistent with theoretical studies which found that helicity cannot cross closed magnetic surfaces in the ideal MHD approximation [19–21].

Low-volume, stellarator-like closed surfaces have been observed in simulations [49, 58]. These surfaces are generated by non-axisymmetric ( $n_\phi = 1$ ) currents outside the closed flux region. Although there has been no systematic study of possible confinement experiments based on these surfaces, there is almost no Ohmic heating inside the closed flux, neoclassical transport may be rapid [58], and the volume outside will not support a hot plasma so this seems unlikely to be a useful confinement configuration.

An alternate approach to good average confinement is termed multipulsing. After formation, the injector current is pulsed to a high level to build a high magnetic field, followed by a current corresponding to the optimum confinement (figure 23) which slowly decays. This is followed by a repeated cycle, etc. If the good-confinement period lasts long enough relative to the building period, average good confinement might be obtained. Initial, two-pulse experiments in SSPX [59] demonstrated the ability to stack pulses, reaching magnetic fields above those from a single, slowly building pulse as seen in figure 27. Simulations showed a very similar behavior [38].

Subsequent experiments [48] applied up to 5 pulses and were capable of more extensive parameter and profile measurements. As seen in figure 28(f), the poloidal magnetic field and other parameters saturated and did not continue to build as additional pulses were added; profiles, e.g. of

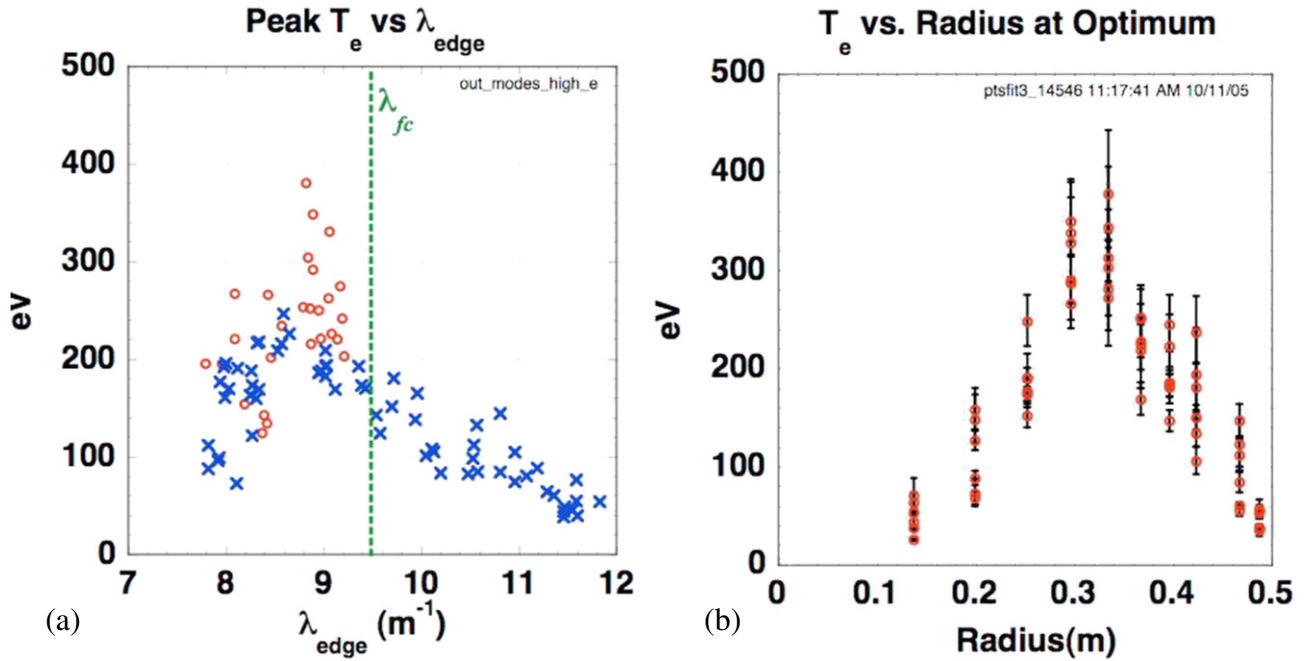


**Figure 23.** (a) Highest  $T_e$  is observed with  $\lambda_{\text{edge}} \approx \lambda_{\text{gun}} < \lambda_{\text{FC}}$ . (b)  $T_e$  profile at maximum available sustainment bank current and optimum  $\lambda_{\text{edge}}$ . The red circles had higher gun current than the blue crosses. From [31].

the safety factor, changed somewhat but probably within the accuracy of the measurements as seen in figure 28(e). Insertable magnetic-probe measurements were consistent with the transient formation of closed surfaces following each current pulse, although the probes' presence in the plasma increased the decay rate of the flux [35].

After the gun current drops below the threshold for driving the  $n_\phi = 1$  mode, the magnetic fluctuations, figure 28(c), are significantly reduced, thus decreasing radial energy transport along magnetic field lines. During these periods the plasma begins to heat, forming a hollow temperature profile with particularly rapid heating locally around 0.26 and 0.42 m. Following a pulse, the fluctuations increase and plasma cools due to transport along open field lines. It should also be noted that the presence of a  $q = 1/2$  surface, figure 28(e), coincides with the occurrence of a hollow temperature profile.

This experiment clearly demonstrated the possibility of using repetitive pulses to sustain a plasma indefinitely. However, it also found that the safety factor and other profiles evolved, becoming unstable during the time between pulses. A detailed, simulation and model study of this effect in the context of achieving long periods of slow relaxation concluded that the duration was limited by the evolution of the  $q$ -profile to an unstable regime [52]. Control of the profile by the edge  $\lambda$  alone was inadequate to extend the confinement period sufficiently for good average energy confinement. Current-profile control is apparently needed for this scenario to succeed.

### 3.8. Pressure limit in a large-aspect ratio spheromak

The flexibility in the bias magnetic field was used to form a large-aspect-ratio spheromak. Spheromaks formed in the bias field configuration 'BCM' (figure 2) had a large current-carrying-hole along the geometric axis resulting in an aspect

ratio of  $\sim 2$ , as seen in figure 29. Large-aspect-ratio spheromaks with no current through the hole ('current-hole spheromaks') have been predicted to have high beta limits [61–63], but no systematic studies exist for cases with current.

The configuration shown in figure 29 was found to be unstable to an  $n_\phi = 2$ ,  $m = 4$  mode at a peak  $\beta = 6\%$  [64]. The high-frequency, magnetic fluctuation level also increased relative to that before the instability onset. At mode onset the density dropped rapidly and the temperature increased over 0.1–0.2 ms, returning  $\beta$  to its original value. Calculation of the Mercier limit for this configuration yielded 6%, in good agreement with this apparent  $\beta$  limit.

The effects of the mode were similar to those at a pressure limit in CTX [65], except that in that experiment the calculated Mercier limit was considerably below the experimental  $\beta$ . The agreement with the Mercier limit in SSPX may have resulted from the increased capabilities to determine and evaluate the plasma characteristics, including the presence and position of a separatrix with gun current flowing in the edge plasma.

### 3.9. Additional physics research

**3.9.1. Hydrogen and deuterium operation.** Comparisons were made between operation of SSPX with deuterium and hydrogen, to see whether differences typical of tokamaks would carry over to spheromaks. No significant difference was found [66].

**3.9.2. Ion temperature measurements.** Ion temperature measurements using an ion-Doppler spectrometer measuring impurity spectra were made during plasma buildup, finding  $T_i \sim 180$  eV [55, 67], consistent with previous results [53, 54, 68]. However, during sustained operation the impurity lines were burned out and the spectrometer was



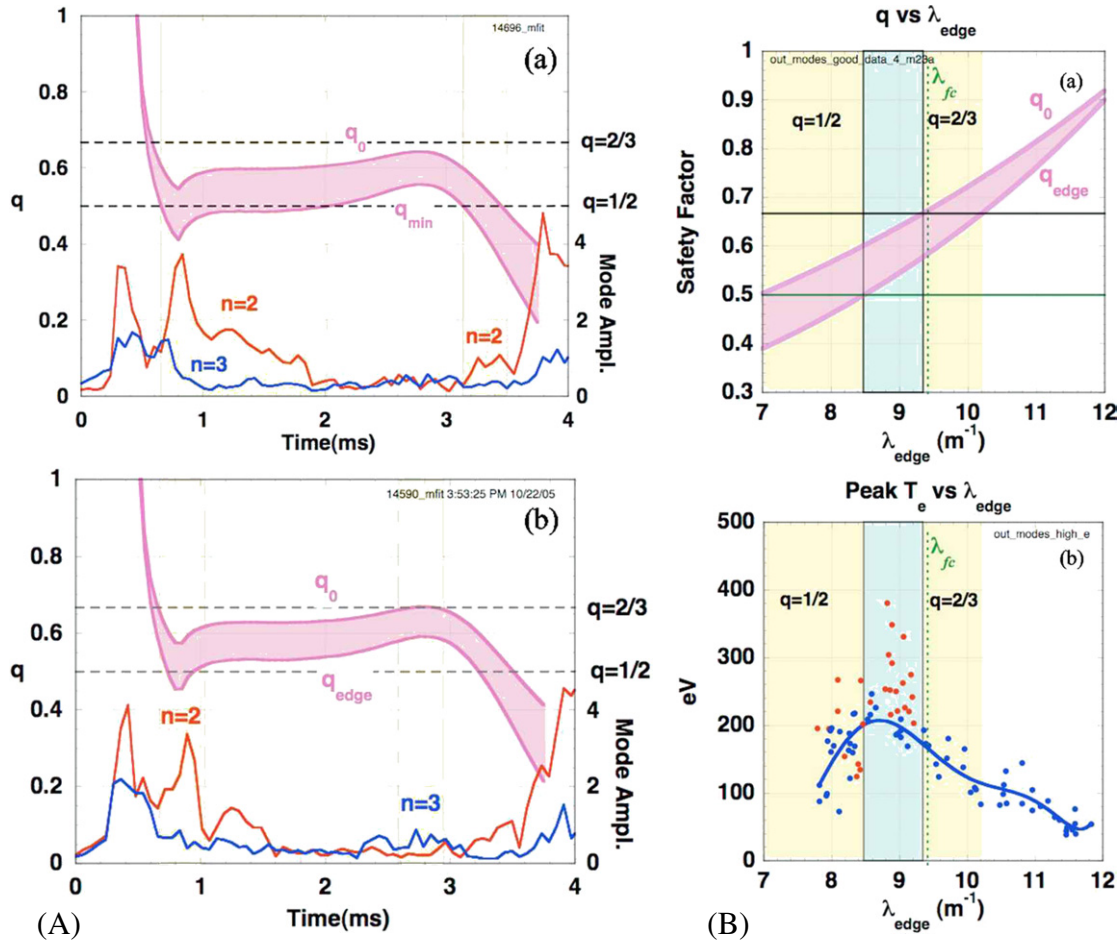


**Figure 24.** (A) The expected modes are observed as the safety factor  $q$  spans different rational surfaces during the discharge. (a) The  $n_\phi = 2$  mode is excited at the beginning and end of the shot. (b)  $q$  is high for this shot, reducing the duration of  $n_\phi = 2$ , but getting high enough at the end to excite the  $n_\phi = 3$  mode. There is a narrow range of quiescent operation. (B) (a) Safety factor versus  $\lambda_{\text{edge}}$  showing stability boundaries for  $m/n_\phi = 1/2, 2/3$  modes. (b) Overlay of stability boundaries on the  $T_e$  data of figure 23 showing high  $T_e$  between the two unstable regions. From [31].

unable to measure temperatures in the spheromak core. Measurements later in the discharge were made using charge-exchange neutrals. The results were consistent with  $T_i \sim T_e$  [56], although the core was well shielded by the dense plasma.

**3.9.3. Helicity balance and transport.** Helicity dissipates in plasmas at a slower rate than energy [17, 18]. Experiments on spheromak buildup using CHI on CTX confirmed this result [69], which is independent of detailed mechanisms, e.g. for driving plasma current. This motivated a study in SSPX on helicity balance in a sustained or slowly decaying spheromak [30], including injection from the gun with corrections for electrode sheath losses, helicity transport into the mean-field spheromak, and the magnetic field and geometry resulting from the Ohmic dissipation of helicity. The gun-injected helicity into the open-field-line region outside the separatrix, and the transport was modeled assuming helicity was a flux function inside the separatrix. Results included the coupling efficiency for transport of helicity from the gun input, defined as

$$\varepsilon_K(\text{sp}) = \left( \frac{dK_{\text{core}}}{dt} + 2 \int_{\text{core}} \eta J \cdot B \, d^3r \right) / (2\psi_{\text{gun}} V_{\text{gun}}). \quad (3)$$

The resulting efficiency, figure 30, ranged from  $<10\%$  to  $\sim 25\%$ , depending on the core (peak)  $T_e$ . Results were shown to be consistent with a hyper-resistivity model [70].

**3.9.4. Atomic spectroscopy.** The SSPX plasma provided a useful tool for determining the atomic spectrum of tungsten for use in the study of a design of an extreme ultraviolet spectrometer for the ITER divertor [71]. Tungsten hexacarbonyl ( $\text{W}(\text{CO})_6$ ) was injected into a 25–100 eV plasma. The resulting spectrum near 150–450 Å was dominated by Er-like W VIII lines with contributions from Tm-like W VI and Ho-like W VIII, many of which were identified by comparison with theory and previous experiments.

**3.9.5. Astronomical physics.** The MHD phenomena observed in SSPX have similarities to astrophysical phenomena, albeit at very different plasma parameters, including coronal mass ejections, reconnection phenomena near the sun and throughout space, and the formation of plasma columns (‘jets’) from the poles of stars and other objects. The latter effect is often accompanied by kinking at considerable distance from the jet origin with the formation of a wide-spread



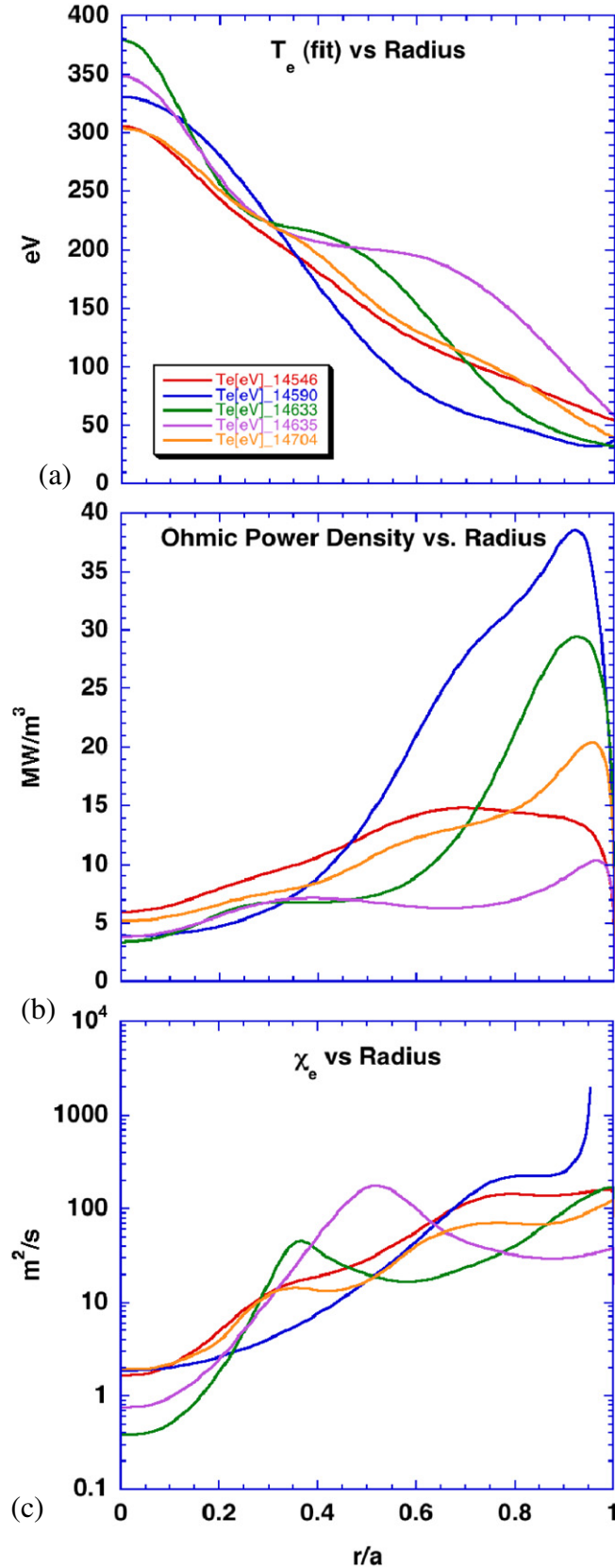


**Figure 25.** Transport properties of SSPX 350 eV shots. (a)  $T_e$ , (b) Ohmic heating density, and (c) thermal diffusivity. From [31].

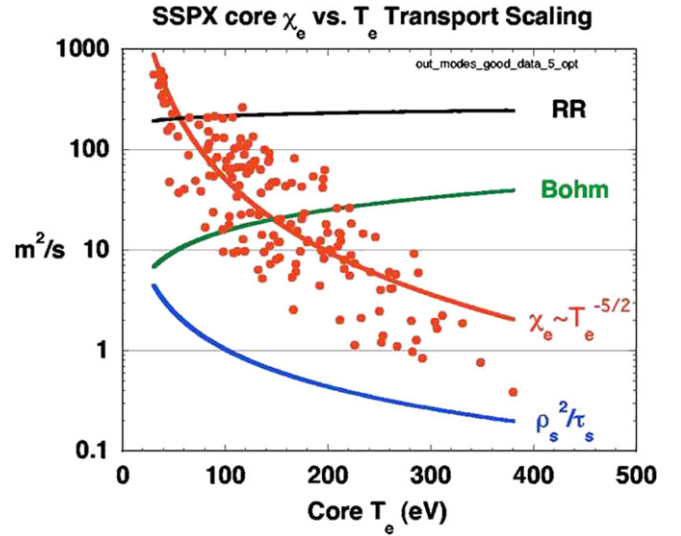


**Figure 26.** Scaling of  $\chi_e$  versus  $T_e$  along with various transport models and power-law best fit through data showing  $\chi_e \sim T_e^{-5/2}$ . 'RR' stands for Rechester–Rosenbluth scaling [57]. From [31].

volume of plasma and magnetic field. The SSPX results have helped guide an ongoing study of cosmic rays formed via jets emanating from black holes, with the basic MHD physics of the effect similar to those seen in early time injection studies in the experiment [72].

#### 4. Discussion and conclusions

SSPX used diagnostics, mostly designed to operate remotely for high-temperature plasmas, coupled to benchmarked, resistive-MHD simulations to provide a quantitative explanation of much of the important physics in a helicity-injected spheromak. The 0.4 keV electron temperature achieved in CTX [73] was exceeded; the conditions to achieve high temperature determined; and the resulting thermal diffusivity measured. The characteristics of the  $n_\phi = 1$  mode associated with CHI were elucidated as was the physics of the nonlinear current drive and magnetic reconnection that form and sustain the spheromak. This work extends previous results; in particular, measurements in SPHEX [74, 75] that demonstrated the role of the  $n_\phi = 1$  mode and in FACT [13] that identified the role of reconnection. The experiments and simulations in SSPX found no path to simultaneous sustainment and good energy confinement.

It was found that reconnection events opened magnetic field lines throughout the spheromak and that the resulting thermal conduction to the walls limited the electron temperatures during sustainment by CHI to less than  $\sim 0.1$  keV. When the drive was reduced below the level that generated magnetic reconnection, the plasma decayed slowly and temperatures as high as 0.5 keV were obtained.

The simulations also accurately calculated the flux and current amplification as a function of the gun current, characterized by the value of  $\lambda_{\text{gun}}$  up to a value of about  $13 \text{ m}^{-1} \approx 1.3\lambda_{\text{FC}}$ . Above this gun current, the experimental flux and current amplification saturated. The saturation

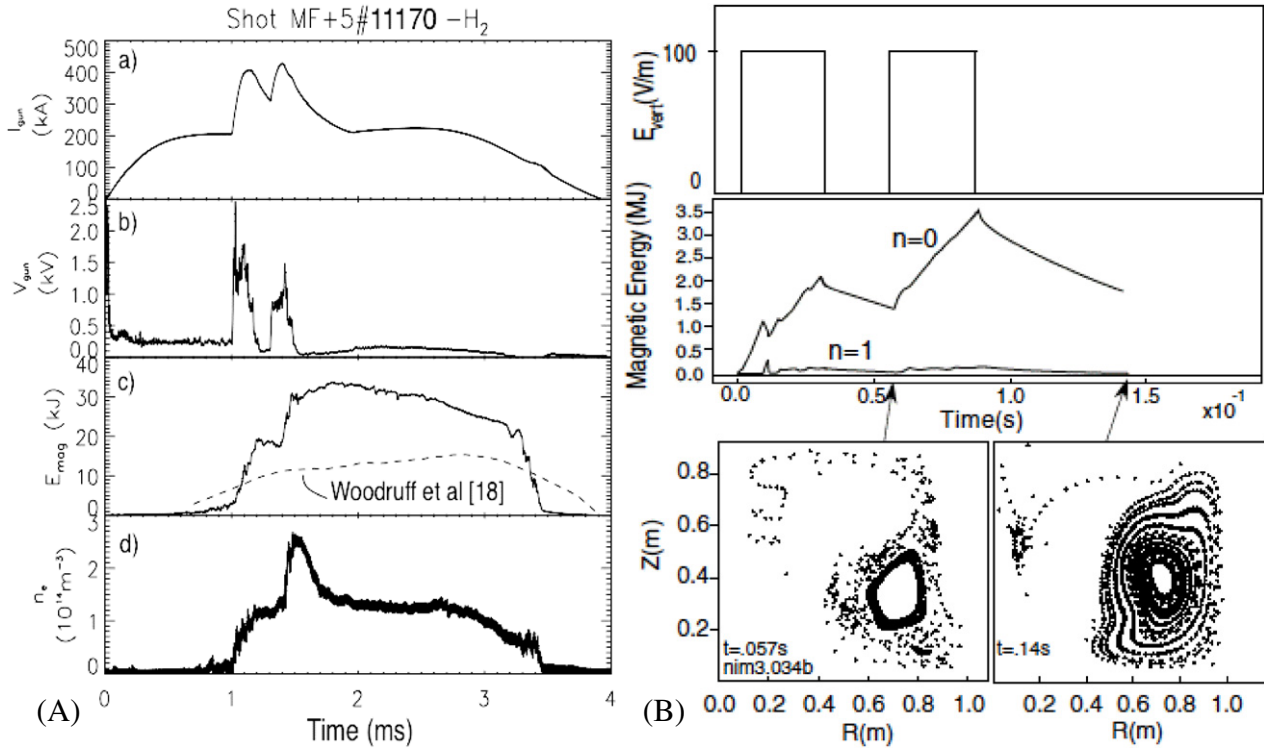


**Figure 27.** (A) Injected current; (b) gun voltage; (c) inferred (using the CORSICA code) magnetic energy content of the spheromak (solid) with magnetic energy evolution from steadily building shots [60] (dashed); and (d) chord-averaged density through the magnetic axis. (B) NIMROD simulations of pulsed operation showing (a) boundary electric field, (b) total magnetic energy, and (c) the growth of regions of closed flux from the first to the second pulse. From [59].

occurred when the amplitude of the  $n_\phi = 1$  mode that generated the magnetic reconnections became large, but the detailed mechanisms apparently lie outside of resistive MHD and are not well understood.

Following the spheromak-buildup phase, the plasma decayed slowly allowing detailed measurements of thermal confinement. The value of  $\lambda$  on the plasma edge, approximately equal to  $\lambda_{\text{gun}}$ , gave a rough control of the  $q$ -profile in the plasma. When it was adjusted to an optimum value,  $q$  became nearly flat. The amplitude of magnetic fluctuations became low resulting in thermal diffusivity in the plasma core  $\sim 1\text{--}10\text{ m}^2\text{ s}^{-1}$ . Use of the edge value of  $\lambda$ , however, was inadequate to provide long-term control of the  $q$ -profile, and it evolved to an unstable state with increased magnetic fluctuations and energy transport. It appears likely that a volumetric  $q$ -profile control mechanism is needed to maintain the high-confinement state for long times.

Extensive experimental exploration of buildup and current sustainment found no conditions with simultaneous good thermal confinement. This result is in agreement with resistive-MHD simulations carried out in support of the experiment and with previously published theoretical calculations [19–21] that found in the ideal MHD approximation there is no transport of helicity across closed magnetic surfaces. The results strongly support the conclusion that coaxial helicity injection as implemented in spheromaks cannot be used for current drive in a steady-state, high-confinement plasma. There are possibilities, however, for long-pulse, high-confinement plasmas with the spheromak periodically rebuilt by helicity

injection. Such plasmas were demonstrated experimentally in SSPX, although the pulse length was limited by the  $q$ -profile evolution.

In summary, the SSPX experiment extended the data base for  $q < 1$  spheromak physics, showing that when the magnetic fluctuation levels are low the thermal diffusivity in the plasma core can be at least comparable to the tokamak L-mode. The buildup and current sustainment by coaxial helicity injection in SSPX degraded thermal confinement by opening the magnetic surfaces during its application, but successfully generated high-quality plasmas used in confinement and other physics studies.

## Acknowledgments

The authors acknowledge contributions from T K Fowler whose ideas stimulated the original SSPX proposal, T R Jarboe who consulted extensively on the design and physics in the early stages of the experiment, D D Ryutov who contributed many important insights and theoretical models to the research, and K I Thomassen who worked to ensure support for the experiment. They also thank many other colleagues and collaborators who made significant contributions to the scientific results and to SSPX experiment and theory, including P M Bellan, D Buchenauer, T A Casper, J H T Clementson, R H Cohen, G A Cone, C W Domier, R W Geer, T Kopriya, R Jayakumar, R O Kemptner, L L LoDestro, M M Marciano, W M Meyer, E D Mezonlin, J M Moller, D D Ryutov, M V Umansky and Z Wang.

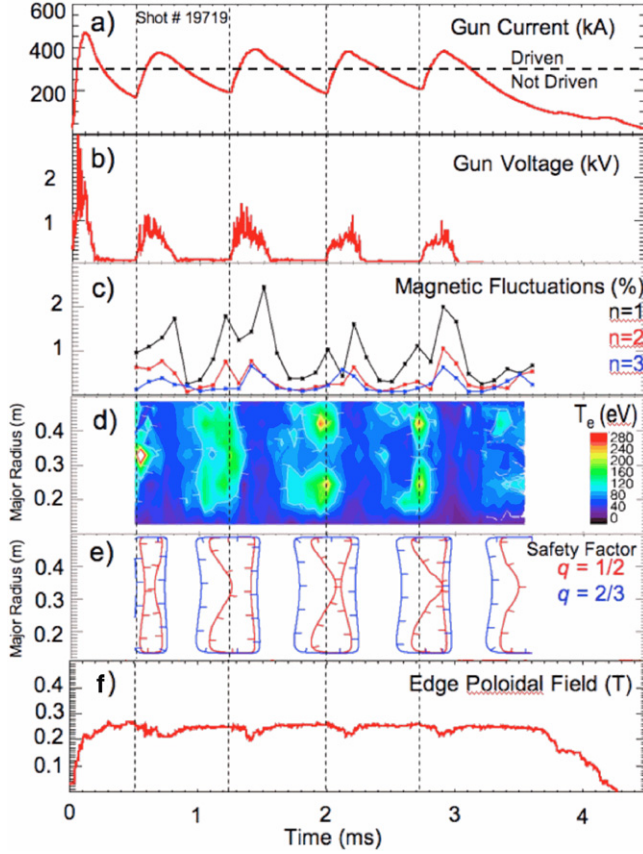


**Figure 28.** Field regeneration multipulse operation. Electron transport during multipulse operation. (a) Gun current. (b) Gun voltage (low when current not driven). (c) Magnetic fluctuations. (d)  $T_e$  scan. (e) Safety factor (hollow  $T_e$  where  $q \sim 1/2$ ). (f) Edge  $B_p$  maintained in quasi-steady state. From [48].

This work was performed under the auspices of the US Department of Energy by Lawrence Livermore National Laboratory under Contract DE-AC52-07NA27344, and by the University of Wisconsin–Madison under Grant No FG02-01ER54661.

## Appendix A. SSPX configuration and operation

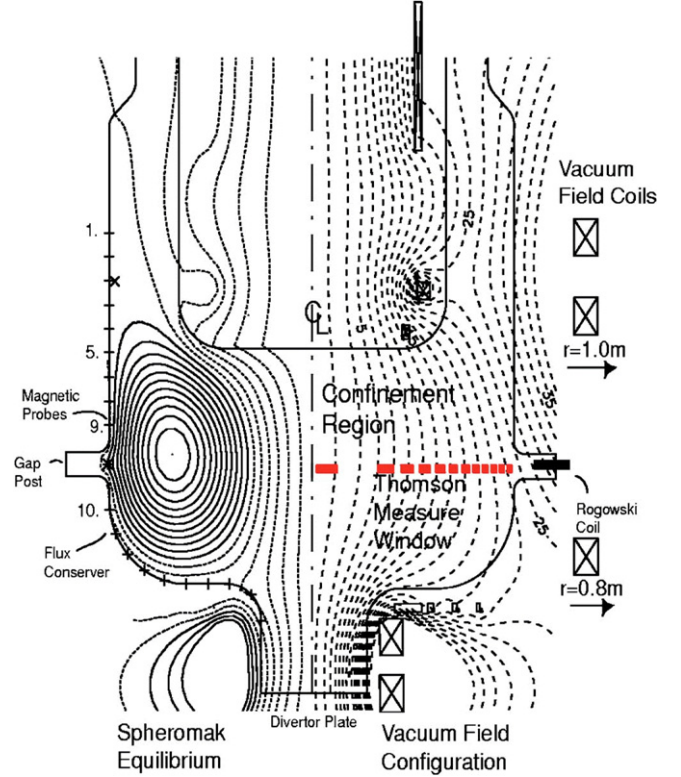
### A.1. Discharge power supplies

Figure A1 is the schematic for the discharge power supplies in their final configuration. ‘PFN’ is a pulse-forming network

### A.2. Vacuum conditions for high-quality discharges

The vacuum vessel and major components had the following volumes: vacuum vessel, 8000 l; flux conserver below the inner electrode, 390 l; coaxial gun region, 160 l (up to gas valves). The system pumping speed was  $1000 \text{ l s}^{-1}$ .

Very clean conditions were achieved by a rigorous program of good vacuum practices, including baking, glow discharge cleaning, and titanium gettering of the flux conserver every third shot [26]. Saturation of the gettered surfaces was readily indicated by increased  $n_e$  and  $H_\alpha$  radiation. Figure A2 shows a time history of the evolution of  $\text{H}_2\text{O}$  in the latter



**Figure 29.** SSPX showing an equilibrium reconstruction for the period during 2/4 activity, and the initial vacuum field configuration on the right. Shown also are the positions of the Thomson temperature measurements. From [64].

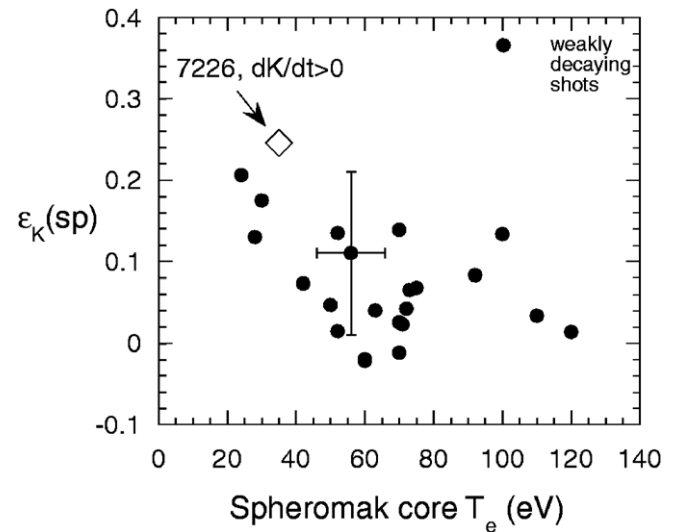


**Figure 30.** Variation with electron temperature of the efficiency  $\varepsilon_K(\text{sp})$  for helicity transport from the gun input into the spheromak core for slowly decaying spheromak plasmas, as inferred from helicity balance. An example for a field-building spheromak is shown for comparison. From [30].

stages of cleaning following a ‘dirty’ vent of SSPX [76]. The helium discharges and gettering were required to reduce impurity levels sufficiently to allow high electron temperatures, as demonstrated in figure A3. The processes also significantly increased the achievable magnetic field in the spheromak (figure A4).



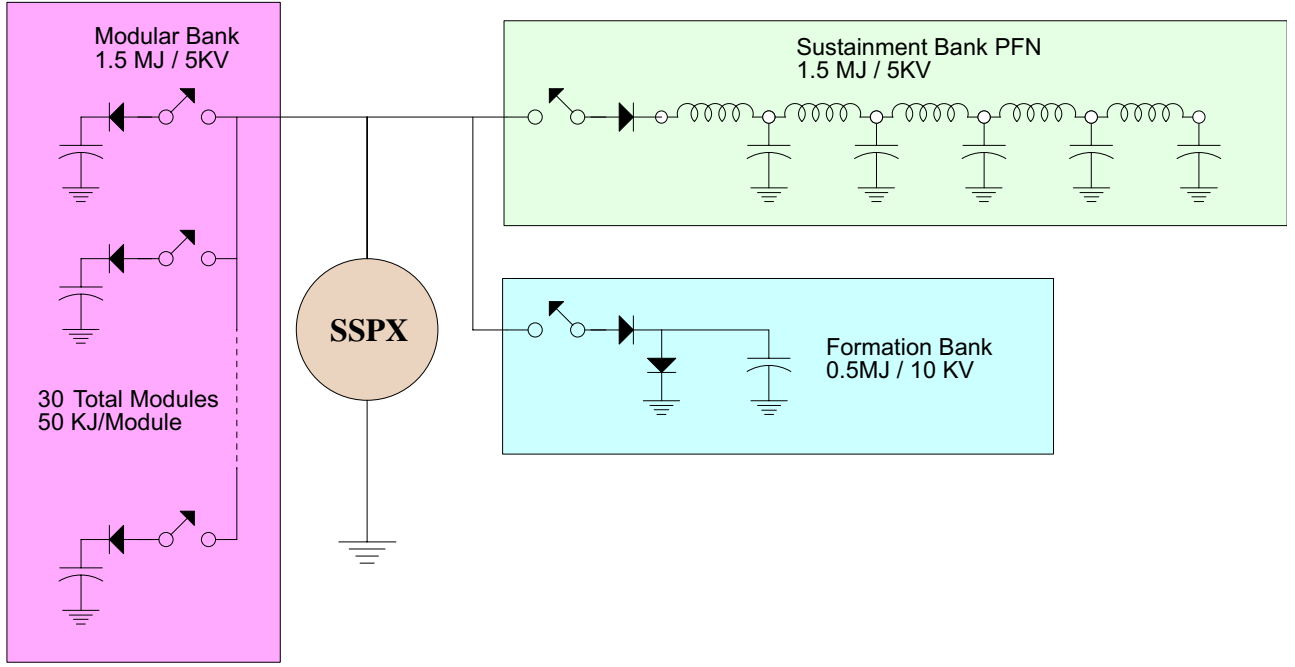


**Figure A1.** Schematic of the SSPX discharge power supplies.

### A.3. Diagnostics

The diagnostics used on SSPX are listed in table 1 together with the properties measured.

## Appendix B. NIMROD simulation model

Simulations of SSPX performed with the NIMROD three-dimensional, nonlinear, time-dependent, resistive magnetohydrodynamic (MHD) code [24] have provided insight into the spheromak formation process, the role of magnetic reconnection in spheromak dynamics, the dynamics of finite amplitude fluctuations during formation, partial sustainment, and decay, energy confinement in the spheromak, and the sensitivity of the energy confinement with respect to the closing and opening of magnetic field lines, as discussed in section 3.3 NIMROD also has been used in validation exercises comparing to SSPX data with increasing fidelity.

The NIMROD nonlinear, resistive-MHD model used in our simulations has been described elsewhere [24, 40, 42]. Resistive MHD combined with collisional transport is a reasonable approximation because the collisional mean-free path is less than or comparable to the axisymmetric flux-conserver radius  $R = 0.5$  m for nominal SSPX plasma parameters on open magnetic field lines with density  $n \sim 5 \times 10^{19} \text{ m}^{-3}$ , electron temperatures  $\sim 35$  eV and singly charged hydrogen ions. Here we briefly review the resistive-MHD NIMROD physics model.

The NIMROD code solves nonlinear time-dependent equations for particle number density ( $n_i = n_e = n$  with quasineutrality), plasma flow velocity ( $V$ ), temperature (assuming  $T_i = T_e = T$ ) and magnetic field ( $B$ ). NIMROD has been used to provide simulation of spheromak plasmas including dynamo, transport and inductive effects without

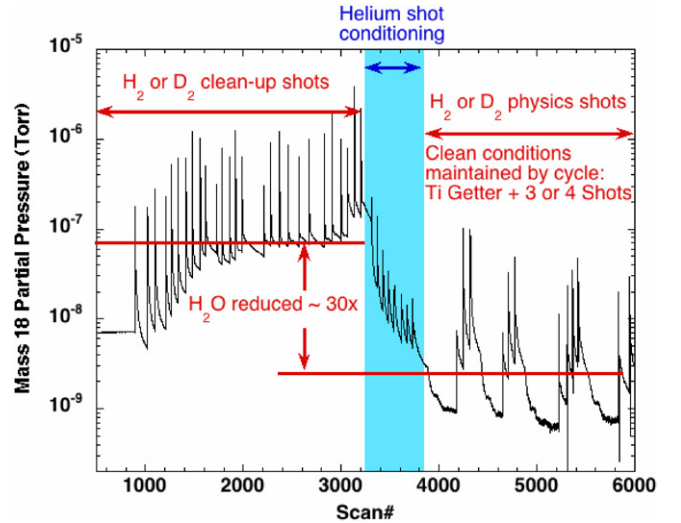


**Figure A2.** Following baking at  $170^\circ\text{C}$  for  $\sim 100$  h and hydrogen glow-discharge cleaning, helium shot conditioning and gettering were used. Shown is the partial pressure of  $\text{H}_2\text{O}$  evolved during the discharges, initially during a series of high-current discharges with hydrogen pulsed from the gas valves (scans 1000–3200) followed by helium discharges without titanium gettering (scans 3200–3800), producing clean conditions for physics shots seen here as cycles of titanium gettering followed by 3–4 discharges (scan 4000–6000). From [26].

resorting to empirical models. In MKS units, the evolution equations are

$$\frac{\partial n}{\partial t} + \nabla \cdot (nV) = \nabla \cdot D \nabla n \quad (1)$$

$$\rho \left( \frac{\partial V}{\partial t} + V \cdot \nabla V \right) = J \times B - \nabla p + \nabla \cdot \rho v \nabla V \quad (2)$$



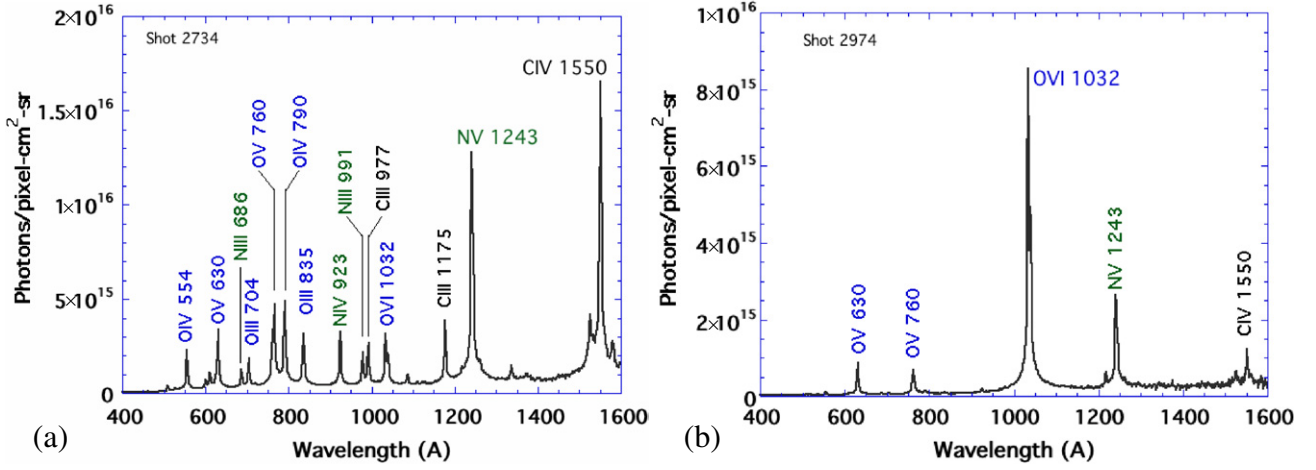


**Figure A3.** VUV spectroscopic measurements without (a) and with (b) helium shot conditioning and gettering. The dominant O VI line at  $\sim 1000 \text{ \AA}$  was indicative of  $T_e > 50 \text{ eV}$  From [76].

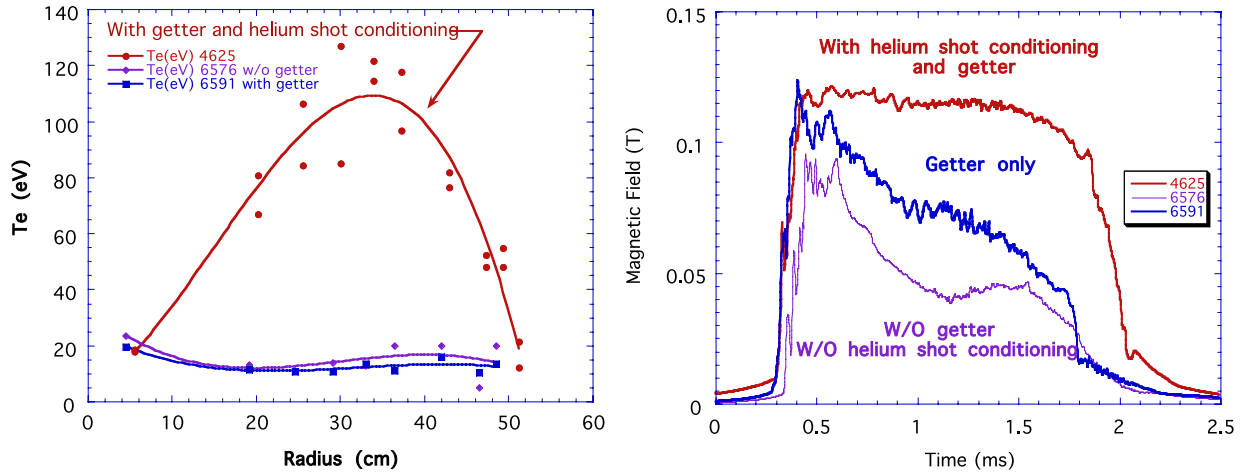


**Figure A4.** Temperatures and magnetic fields with and without the full cleaning scenario. Good discharges resulted from the cleaning as evidenced by peaked electron temperature measurements (a) and considerably increased magnetic field decay times (b). From [76].

$$\frac{nk_B}{\gamma - 1} \left( \frac{\partial T}{\partial t} + \mathbf{V} \cdot \nabla T \right) = -\frac{p}{2} \nabla \cdot \mathbf{V} + \nabla \cdot nk_B [\chi_{\parallel} \hat{\mathbf{b}} \hat{\mathbf{b}} + \chi_{\perp} (\mathbf{I} - \hat{\mathbf{b}} \hat{\mathbf{b}})] \cdot \nabla T + \frac{\eta J^2}{2} \quad (3)$$

$$\frac{\partial \mathbf{B}}{\partial t} = \nabla \times (\mathbf{V} \times \mathbf{B} - \eta \mathbf{J}) \quad (4)$$

$$\mu_0 \mathbf{J} = \nabla \times \mathbf{B}, \quad (5)$$

where  $p = 2nk_B T$  is the sum of electron and ion pressures, and  $\hat{\mathbf{b}} \equiv \mathbf{B}/|\mathbf{B}|$  is the unit vector for the magnetic field. The simulations consider  $n$ ,  $T$ ,  $\mathbf{V}$ ,  $\mathbf{B}$  and  $\mathbf{J}$  to be functions of all three spatial dimensions and time. Thus, induction effects on the spheromak equilibrium due to magnetic fluctuations and energy transport from heat-flow fluctuations are modeled explicitly. The boundary conditions are  $\mathbf{E} \times \hat{\mathbf{n}} = \delta \mathbf{B} \cdot \hat{\mathbf{n}} = \nabla n \cdot \hat{\mathbf{n}} = T = 0$  and  $\mathbf{v} = 0$  (in the absence of imposed rotation) on the conducting surfaces, where  $\mathbf{B} = \mathbf{B}_{\text{vac}} + \delta \mathbf{B}$ . The vacuum magnetic field  $\mathbf{B}_{\text{vac}}$  from coils are assumed to have

soaked through the bounding surfaces and is static. Rotation is introduced with a boundary condition on the fluid velocity.

The parallel thermal diffusivity is  $\chi_{\parallel} = 387T^{5/2} \text{ m}^2 \text{ s}^{-1}$  [77, 78]. In many of the calculations targeting simulation of SSPX plasmas we have set the perpendicular thermal diffusivity  $\chi_{\perp} = 21 \text{ m}^2 \text{ s}^{-1}$  motivated by experimental measurements and calculations with the CORSICA transport and equilibrium code [31]. We use the core thermal conductivity found by fitting the data in this axisymmetric approximation; in our simulations a large thermal transport arises near the edge from the large parallel thermal conductivity in the presence of stochastic field lines. The magnetic diffusivity has sometimes been set to a constant value appropriate for some reference electron temperature but is more often computed as  $\eta/\mu_0 = 411(1 \text{ eV}/T)^{3/2} \text{ m}^2 \text{ s}^{-1}$ , using the toroidally averaged temperature [38, 41, 42].

Many of the simulations have used constant isotropic viscosity  $\nu = 1000 \text{ m}^2 \text{ s}^{-1}$  to provide nonlinear numerical stability during the full-power stage of the current drive. With temperatures of approximately 30 eV in the edge plasma or during the spheromak formation stage, and up to a peak of  $\sim 500 \text{ eV}$  in simulations of decay, the Lundquist number

**Table 1.** SSPX diagnostics.

Diagnostic	Measures	Time resolution	Spatial profile
Profile Thomson scattering	$n_e, T_e$	Gated-single point measurement	10 points
CO <sub>2</sub> Laser	$n_e$	Yes	2 chords
16 channel Photodiode bolometer array	Power radiated ( $P_{\text{rad}}$ ), energy ( $W_{\text{rad}}$ ) loss distribution	Yes	Yes
3 channel filtered bolometer array	$P_{\text{rad}}$ and $W_{\text{rad}}$	Yes	Views midplane
1 channel thermistor	$W_{\text{rad}}$	Integrating	Views midplane
SPRED spectrometer	$W_{\text{rad}}, T_e$ , spectral rad	Integrating	Single chord, can be scanned
Ion-Doppler spectrometer [67]	$T_i$ , drift velocity	Yes	Views 1 of 5 selectable chords
Charge-exchange particle neutral analyzer [56]	$T_i$	Yes	No
Wall magnetic probes	Poloidal and toroidal magnetic field at wall	Yes	Wall profile in $z$ , azimuthal angle
Flux-conserver Rogowski coils	Current in flux-conserver posts	Yes	Profile in azimuthal angle
Insertable magnetic probes [33, 35]	Local magnetic field	Yes	Yes
Visible Spectrometer	Impurities	Integrating	Single chord
Hard x-ray	Runaway electrons	Yes	3 azimuthal locations at midplane
VUV monochrometers	Line ratios, impurities, $T_e$	Yes	two chords
Midplane H-alpha array	Neutral H	Yes	7 chords
Injector H-alpha	Neutral H	Yes	Single chord
Injector TV camera	Discharge visible light	Gated-single point	Yes
Midplane TV camera [81]	Discharge visible light	Gated-single point	Yes
Discharge bank Rogowskis coils	Capacitor bank current, input power	Yes	NA
Injector voltage	Injector voltage, input power	Yes	NA
Bank room TV camera	Monitors for arcs	Yes	NA
Injector room TV camera	Monitors for arcs	Yes	NA
Residual gas analyzer	Vacuum system-H <sub>2</sub> O, evolved gas	Yes	NA
Vessel pressure	Vacuum system, gas valve ops	Yes	NA

(computed as  $S = \mu_0 R v_A / \eta$ , where  $R$  is the major radius of the SSPX flux conserver and  $v_A$  is the Alfvén speed) is of order  $10^5$ – $10^6$  at the peak  $T_e$ . The magnetic Prandtl number ( $P_m \equiv \nu \mu_0 / \eta$ ) is large for nonlinear numerical stability purposes [24, 40]; thus,  $P_m \sim 10^2$ – $10^3$  at peak  $T_e$  and  $\sim 10$ – $10^2$  on and near the open-field line edge. The diffusion term in equation (1) keeps the density relatively smooth in the absence of particle transport and atomic fueling effects that are poorly understood and not present in the MHD model. The value of the artificial diffusivity ( $D = 10^4 \text{ m}^2 \text{ s}^{-1}$ ) is selected to help keep the computed minimum of the number density field above zero during strong drive when the MHD activity is violent. For the same reason, the diffusivity is increased locally in computational cells where  $n$  falls to 3% of its volume-averaged value. Use of the artificial density diffusivity alters the physics of the simulation in a limited way [79], including energy conservation [42, 79]. As the radiation power is small compared with Ohmic power in most SSPX shots after proper wall conditioning, radiation has not been modeled in the NIMROD simulations.

Because the SSPX magnetic helicity was injected from a coaxial plasma gun connected to a capacitor bank that provided a current source, a multi-element capacitor bank was modeled as an external circuit for the NIMROD simulations [38, 39]. The numerical model for the capacitor bank mimicked the actual programming of the experimental bank. The geometry of the simulation domain was defined to match the main characteristics of the SSPX configuration.

In a gun-driven spheromak, plasma, current and magnetic flux are pushed out of the coaxial plasma gun into the flux conserver by  $\mathbf{J} \times \mathbf{B}$  forces [15, 16, 35, 36, 40, 80]. The studies of Finn *et al* [40, 58] used a resistive-MHD model and the NIMROD code to study a spheromak plasma driven by a voltage source in a simplified cylindrical system (flux core) and in a gun geometry. This work established the importance of the  $n_\phi = 1$  kink mode driven unstable by the central current column. When the voltage source was just a little larger than a critical value, a significant volume of closed magnetic field lines could be created. At higher voltages, the kink mode was driven harder; the volume of open field lines increased; and the relative volume of closed flux became small. For even higher voltages a limit-cycle behavior was observed.

The work of Sovinec *et al* [41] investigated the role of transient effects in SSPX energy confinement. In this work the resistive-MHD equations were solved in NIMROD with temperature-dependent thermal conduction and electrical resistivity in the SSPX vacuum chamber geometry with an applied simulated injector-current waveform that approximated specific SSPX discharges Nos 4620–4662 [36]. These studies illustrated the tight coupling of the temperature and magnetic fields: magnetic topology and parallel thermal conduction regulate energy confinement, while resistivity influences magnetic reconnection and diffusion. The length of open magnetic field lines and the extent of any region of closed magnetic flux are governed dynamically by MHD instabilities, which respond quickly to

changes in the parallel current density distribution. The work in [38–41, 80] and in other studies confirmed that the gun-driven plasma develops the  $n_\phi = 1$  kink mode of the central current column leading to formation of the poloidal magnetic field and relaxation into a spheromak.

## References

- [1] Alfvén H, Lindberg L and Mitlid P 1960 *J. Nucl. Energy, Part C: Plasma Phys.* **1** 116
- [2] Bussac M N, Furth H P, Okabayashi M, Rosenbluth M N and Todd A M N 1979 *Plasma Physics and Controlled Nuclear Fusion Research 1978* vol III (Vienna: IAEA) p 249
- [3] Rosenbluth M N and Bussac M N 1987 *Nucl. Fusion* **19** 489
- [4] Yamada M, Furth H P, Hsu W, Janos A, Jardin S, Okabayashi M, Sennis J, Stix T H and Yamazaki K 1981 *Phys. Rev. Lett.* **46** 188
- [5] Goldenbaum G C, Irby J H, Chong Y P and Hart G W 1980 *Phys. Rev. Lett.* **44** 393
- [6] Yasuyuki N, Hiroki O, Yukio O, Katsunori S and Hisamitsu Y 1980 *J. Phys. Soc. Japan* **49** 710
- [7] Turner W C, Granneman E H A, Hartman C W, Prono D S, Taska J and Smith A C Jr 1981 *J. Appl. Phys.* **52** 175
- [8] Jarboe T R, Henins I, Sherwood A R, Barnes C W and Hoida H W 1982 *Phys. Rev. Lett.* **51** 39
- [9] Watanabe K, Ikegami I, Ozaki A, Satomi N and Uyama T 1981 *J. Phys. Soc. Japan* **50** 1823
- [10] Kawai K, Pietrzyk Z A and Hunter H T 1987 *Phys. Fluids* **30** 2561
- [11] Jarboe T R, Barnes C W, Platts D A and Wright B L 1985 *Comment. Plasma Phys. Control. Fusion* **9** 161
- [12] Rusbridge M G, Gee S J, Browning P K, Cunningham C, Duck R C, al-Karthy A, Martin R and Bradley J W 1997 *Plasma Phys. Control. Fusion* **39** 683
- [13] Nagata M, Kanki T, Masuda T, Naito S, Tatsumi H and Uyama T 1993 *Phys. Rev. Lett.* **71** 4342
- [14] Jarboe T R *et al* 2011 *Nucl. Fusion* **51** 063029
- [15] Jarboe T R 1994 *Plasma Phys. Control. Fusion* **36** 945
- [16] Bellan P M 2000 *Spheromaks* (London: Imperial College Press,)
- [17] Taylor J B 1974 *Phys. Rev. Lett.* **33** 1139
- [18] Taylor J B 1986 *Rev. Mod. Phys.* **58** 741
- [19] Boozer A H 1993 *Phys. Fluids B* **5** 2271
- [20] Moses R W, Gerwin R A and Schoenberg K F 2001 *Phys. Plasmas* **8** 4839
- [21] Mett R R and Taylor J B 1992 *Phys. Fluids B* **4** 73
- [22] Crotinger J A, LoDestro L, Pearlstein L D, Tarditi A, Casper T A and Hooper E B 1997 Corsica: a comprehensive simulation of toroidal magnetic-fusion devices LLNL Report UCRL-ID-126284
- [23] Hooper E B, Pearlstein L D and Bulmer R H 1999 *Nucl. Fusion* **39** 863
- [24] Sovinec C R, Glasser A H, Gianakon T A, Barnes D C, Nebel R A, Kruger S E, Schnack D D, Plimpton S J, Tarditi A, Chu M S and the NIMROD Team 2004 *J. Comput. Phys.* **195** 355
- [25] Buchenauer D A, Mills B E, Wood R, Woodruff S, Hill D N, Hooper E B, Cwiggill D F, Clift M W and Yang N Y 2001 *J. Nucl. Mater.* **290–293** 1165
- [26] Wood, R D, Hill D N, Hooper E B, Buchenauer D, McLean H, Wang Z, Woodruff S and Wurden G 2001 *J. Nucl. Mater.* **290–293** 513
- [27] Hill D N, Wood R D, Bulmer R, McLean H S, Ryutov D, Stallard B W and Woodruff S 2003 *J. Nucl. Mater.* **313–316** 941
- [28] Jarboe T R 1989 *Fusion Technol.* **15** 7
- [29] McLean H S *et al* and the SSPX Team 2001 *Rev. Sci. Instrum.* **72** 556
- [30] Stallard B W, Hooper E B, Woodruff S, Bulmer R H, Hill D N, McLean H S, Wood R D and the SSPX Team 2003 *Phys. Plasmas* **10** 2912
- [31] McLean H S, Wood R D, Cohen B I, Hooper E B, Hill D N, Moller J M, Romero-Talamás C and Woodruff S 2006 *Phys. Plasmas* **13** 056105
- [32] Knox S O, Barnes C W, Marklin G J, Jarboe T R, Henins I, Hoida H W and Wright B L 1986 *Phys. Rev. Lett.* **56** 842
- [33] Holcomb C T, Jarboe T R, Hill D N, Woodruff S and Wood R W 2006 *Phys. Plasmas* **13** 022504
- [34] Cohen B I, Romero-Talamás C A, Ryutov D D, Hooper E B, LoDestro L L, McLean H S, Stewart T L and Wood R D 2009 *Phys. Plasmas* **16** 042501
- [35] Romero-Talamas C A, Hooper E B, Jayakumar R, McLean H S, Wood R D and Moller J M 2008 *Phys. Plasmas* **15** 042503
- [36] Romero-Talamas C A, Holcomb C, Bellan P M and Hill D N 2006 *Phys. Plasmas* **13** 022502
- [37] Wood R D *et al* 2005 *Nucl. Fusion* **45** 1582
- [38] Cohen B I, Hooper E B, Cohen R H, Hill D N, McLean H S, Wood R D, Woodruff S, Sovinec C R and Cone G A 2005 *Phys. Plasmas* **12** 056106
- [39] Hooper E B, Kopriva T A, Cohen B I, Hill D N, McLean H S, Wood R D and Woodruff S 2005 *Phys. Plasmas* **12** 092503
- [40] Sovinec C R, Finn J M and del-Castillo-Negrete D 2001 *Phys. Plasmas* **8** 475
- [41] Sovinec C R, Cohen B I, Cone G A, Hooper E B and McLean H S 2005 *Phys. Rev. Lett.* **94** 35003
- [42] Hooper E B, Cohen B I, McLean H S, Wood R D, Romero-Talamas C A and Sovinec C R 2008 *Phys. Plasmas* **15** 032502
- [43] Wood R D, Hill D N, McLean H S, Hooper E B, Hudson B F and Moller J M 2009 *Nucl. Fusion* **49** 025001
- [44] Ryutov D D, Cohen R H and Hill D N 2003 *Plasma Phys. Rep.* **29** 605
- [45] Huang Y-M, Bhattacharjee A and Sullivan B P 2011 *Phys. Plasmas* **18** 072109
- [46] Hooper E B, Cohen B I, Hill D N, LoDestro L L, McLean H S, Romero-Talamás C A, Wood R D and Sovinec C R 2007 *J. Fusion Energy* **26** 71
- [47] Hooper E B, Hill D N, McLean H S, Romero-Talamás C A and Wood R D 2007 *Nucl. Fusion* **47** 1064
- [48] Hudson B *et al* 2008 *Phys. Plasmas* **15** 056112
- [49] Hooper E B, Romero-Talamás C A, LoDestro L L, Wood R D and McLean H S 2009 *Phys. Plasmas* **16** 052506
- [50] Kitson D A and Browning P K 1990 *Plasma Phys. Control. Fusion* **32** 1265–87
- [51] McLean H S, Woodruff S, Hooper E B, Bulmer R H, Hill D N, Holcomb C, Moller J, Stallard B W, Wood R D and Wang Z 2002 *Phys. Rev. Lett.* **88** 125004
- [52] Hooper E B 2011 *Plasma Phys. Control. Fusion* **53** 085008
- [53] Fernandez J C, Barnes C W, Jarboe T R, Henins I, Hoida H W, Klingner P L, Knox S O, Marklin G J and Wright B L 1988 *Nucl. Fusion* **28** 1555
- [54] Gibson K J, Gee S G and Rusbridge M G 1995 *Plasma Phys. Control. Fusion* **37** 31
- [55] Auerbach D W, Hill D N, McLean H S and the SSPX Team 2000 *Bull. Am. Phys. Soc.* **45** 245
- [56] Mezonlin E D *et al* 2007 *Rev. Sci. Instrum.* **78** 053504
- [57] Rechester A B and Rosenbluth M N 1978 *Phys. Rev. Lett.* **40** 38
- [58] Finn J M, Sovinec C R and del-Castillo-Negrete D 2000 *Phys. Rev. Lett.* **85** 4538
- [59] Woodruff S, Stallard B W, McLean H S, Hooper E B, Bulmer R, Cohen B I, Hill D N, Holcomb C T, Moller J and Wood R D 2004 *Phys. Rev. Lett.* **93** 205002
- [60] Woodruff S, Hill D N, Stallard B W, Bulmer R, Cohen B, Holcomb C T, Hooper E B, McLean H S, Moller J and Wood R D 2003 *Phys. Rev. Lett.* **90** 095001



- [61] Gautier P, Gruber R and Troyon F 1981 *Nucl. Fusion* **21** 1399
- [62] Jardin S C 1982 *Nucl. Fusion* **22** 629
- [63] Mayo R M and Marklin G J 1988 *Phys. Fluids* **31** 1812
- [64] Woodruff S, Hooper E B, Pearlstein L D, Bulmer R, Hill D N, Holcomb C T, McLean H S, Moller J, Stallard B W and Wood R D 2006 *Phys. Plasmas* **13** 044506
- [65] Wysocki F J, Fernández, Henins I, Jarboe T R and Marklin G J 1988 *Phys. Rev. Lett.* **61** 2457
- [66] Wood R D, Ryutov D, Hill D N, McLean H s and Woodruff S 2003 *Bull. Am. Phys. Soc.* **48** 151
- [67] Auerbach D 2003 Ion temperature measurements in SSPX *Senior Thesis* Swarthmore College of Physics
- [68] Mayo R M, Fernández J C, Henins I, Kirschenbaum L S, Munson C P and Wysocki F J 1991 *Nucl. Fusion* **31** 2087
- [69] Barnes C W, Fernández J C, Henins I, Hoida H W, Jarboe T R, Knox S O, Marklin G J and McKenna K F 1986 *Phys. Fluids* **29** 3415
- [70] Hooper E B and Pearlstein L D 2002 *Plasma Phys. Rep.* **28** 765
- [71] Clementson J, Beirsdorfer P, Magee E W, McLean H S and Wood R D 2010 *J. Phys. B: At. Mol. Opt. Phys.* **43** 144009
- [72] Fowler T K, Colgate S, Li H, Bulmer R H and Pino J 2011 On the origin of ultra high energy cosmic rays II *Lawrence Livermore National Laboratory Report LLNL-TR-474338* 27 March
- [73] Jarboe T R, Wysocki F J, Fernández J C, Henins I and Marklin G J 1990 *Phys. Fluids B* **2** 1342
- [74] al-Karkhy A, Browning P K, Cunningham G, Gee S J and Rusbridge M G 1993 *Phys. Rev. Lett.* **70** 1814
- [75] Duck R C, Browning P K, Cunningham G, Gee S J, al-Karkhy A, Martin R and Rushbridge M G 1997 *Plasma Phys. Control Fusion* **39** 715
- [76] Wood R G, Hill D N and the SSPX Team 2001 *Bull. Am. Phys. Soc.* **46** 158
- [77] Spitzer L 1965 *Physics of Fully Ionized Gases* 2nd rev. edn (New York: Interscience Publication) pp 136–46
- [78] Braginskii S I 1965 *Reviews of Plasma Physics* vol 1, ed M A Leontovich (New York: Consultants Bureau) p 205
- [79] Ryutov D D, Cohen B I, Cohen R H, Hooper E B and Sovinec C R 2005 *Phys. Plasmas* **12** 084504
- [80] Jarboe T R, Henins I, Sherwood A R, Barnes C W and Hoida H W 1983 *Phys. Rev. Lett.* **51** 39
- [81] Romero-Talamás C A 2005 Investigations of spheromak plasma dynamics: high-speed imaging at the sustained spheromak physics experiment and magnetic diagnostics at the Caltech spheromak experiment *PhD Thesis* California Institute of Technology, Pasadena, CA